공학박사 학위논문

Preparation and Investigation of Synthetic Carbon Nanosheets and Copper (II)-Polydopamine for Hydrogen Production

탄소 나노 시트 및 구리 이온 함유
폴리도파민의 수소 생산 촉매 합성 및 연구

2018년 2월

서울대학교 대학원
재료공학부
안중현

Abstract

Preparation and Investigation of Synthetic Carbon Nanosheets and Copper (II)-Polydopamine for Hydrogen Production

Junghyun An
Department of Materials Science and Engineering
College of Engineering
Seoul National University

The development of efficient co-catalysts indicates one of the most significant topics for the commercialization of photoelectrochemical hydrogen evolution. The design and preparation of carbon-based catalysts is a significant research part for inexpensive, environment-friendly, and durable catalysts that may replace previously developed noble metal catalysts. Nevertheless, the challenge associated with the previous carbon-based catalysts, such as graphene and graphene-based materials, lies in the complicated and inefficient synthetic processes.

As the simplest model carbon-based platform, CVD-monolayer graphene was chosen as a HER catalyst. Graphene possesses excellent transmittance and superior intrinsic carrier mobility. For the first time, we have investigated

new possibilities of monolayer graphene as the efficient HER catalyst. The catalytic activity can be further enhanced by generating more active sites. Treatment with N_2 plasma also induces N doping and abundant defects. The catalyst exhibits a lower Tafel slope (45 mV/decade) and a higher exchange current density (7.1×10^{-5} mA/cm^2) than those of other previously reported carbon-based HER catalysts, indicating performance comparable to that of Pt catalyst. Based on the electrochemical analysis, the active sites of the N-doped graphene have been identified and quantified.

Moreover, another type of the biomimetic carbon-based nanosheets is addressed as a new HER catalyst. Here, inspired by biomolecular system based on mussel adhesive protein, we prepared transition metal-complexed PDA matrix (M-PDA) as a new hydrogen evolution catalyst and investigated HER catalytic properties in neutral pH condition. Through oxidative polymerization of dopamine, we synthesized PDA with various transition metal such as Co^{2+}, Cu^{2+}, Mn^{2+}, Ni^{2+}, and Fe^{3+} ion. Moreover, Cu(II)-PDA complex show the lowest overpotential for HER among these M-PDAs. To the best of our knowledge, there is no previous studies on the application of biomimetic PDA derivatives to hydrogen production catalysts, and the overpotential of Cu(II)-PDA is lowest value among copper-based electrocatalysts for hydrogen production. This significant enhancement achieved in this study emphasizes the new possibilities for the application of bioinspired materials as hydrogen evolution reaction catalyst as well as molecular precursor approach.

Keywords: photoelectrochemical silicon cell, carbon-based catalyst, bioinspired, Dopamine, water splitting, hydrogen production
Student Number: 2012-30162

Contents

List of Tables

List of Figures

Chapter 1. Introduction

1.1 Energy demand for renewable energy source

The end of the oil age is approaching. Prior to the 21st century, energy supply was mainly utilized by fossil fuels and nuclear energy. As the human civilization development, energy consumption began to increase exponentially. However, these energy sources each have major disadvantages, for example, damage of oil shock, global warming due to carbon dioxide emissions and possible disasters caused by nuclear energy malfunctions as shown in Chernobyl and Fukushima nuclear accident.[1.1-1.5] Especially in Korea, many people suffered from fine dust this year, and in 2016, the earthquake of Gyeongju caused anxiety about nuclear safety. Therefore, Development of renewable and eco-friendly energy sources are globally main issues to find solution for increase of energy consumption and safety.[1.6-1.8] The world energy consumption rate is projected to double from 13.5 TW in 2001 to 27 TW by 2050 and to triple to 43 TW by 2100.[1.9]. In early 2000, Germany enforced a denuclearization policy, with the result that wind, solar, and bioenergy accounted for about 30% of the current electricity supply. They assumed a technical alternative, e.g. Power-to-Gas (P2G), and a battery in an electric vehicle to overcome the shortcomings of power generation, which is the biggest shortcoming of renewable energy. Thus, many researchers have been trying to multifariously develop sustainable energy sources, such as solar, wind, biomass, biofuel, geothermal and hydrogen. Nowdays, renewable energy market is expanding rapidly, renewable energy facilities are increasing by 9% a year. Thus, renewable energy has already overtaken fossil fuel and nuclear power generation and has become a leader in the international energy market.

Among the sustainable energy, hydrogen gas is the most suitable element that can be utilized as an energy source for fuel cells. Hydrogen is an ideal

fuel source because when it is used, by-products are water, heat and electricity without CO_2 emission. Hydrogen is also non-toxic while nuclear energy, coal, and gasoline are all either toxic or hazardous to the environment. Moreover, hydrogen energy is a very efficient fuel source compared to traditional sources of energy. The use of hydrogen as an energy source can be linked to the decarbonization of the energy concept, and that in 2100 it is expected to take the market as the main energy source. The global fuel cell market is on the rise and the global fuel cell market is about $ 3.6 billion by 2015. Worldwide fuel cell system sales have increased by about 12%. In order to develop hydrogen production as sustainable energy source, it is important to secure the cleanliness of hydrogen production. In the short term, it is necessary to connect with energy-related technologies. In the long term, it is desirable to use hydrogen as renewable energy.

1.2 Hydrogen evolution reaction (HER)

General description of HER and catalyst for HER

The hydrogen production from water is considered as one of sustainable energy sources and important solution of future energy deficiency. However, the development of an effective electrochemical catalyst for hydrogen production is still under study. Waters plitting for hydrogen production consists basically of two oxidation-reduction reactions.

The oxidation reaction in the electrolysis of water is:

$O_2 + 4e^- + 4H^+ \leftrightarrow 2H_2O$ $E_{anodic} = 1.23\ V - 0.059(pH)\ V$ (vs. NHE) (1.1)

while the reduction reaction is:

$4e^- + 4H^+ \leftrightarrow 2H_2$ $E_{cathodic} = 0\ V - 0.059(pH)\ V$ (vs. NHE) (1.2)

, where NHE is the Normal Hydrogen Electrode. The value of standard potential is varied by pH ($E_{half\ reaction} = E - 0.059 * (pH)$ vs NHE). The thermodynamic potential of the water splitting reaction ($E_{o,cell} = 1.23$ V) is calculated from the difference between the equation (2) and (1). However, additional potential is kinetically required to generate a reaction at a certain rate, which is called overpotential, η. Whereas, if a current icathodic flows at the cathode, the same current of ianodic has to flow at the anode side to connect the circuit. Therefore, both the anode and cathode electrodes need the additional overpotential. The overpotentials at the both electrode are expressed as η_c and η_a, respectively. Therefore, the overall applied potential, Eapplied potential, is

$E_{appl} = 1.23V + \eta_c + \eta_a$ (1.3)

Higher overpotential requires higher total applied voltage. Using an electrocatalyst for water splitting can reduce the overpotential required for electrolysis of water.

The hydrogen evolution reaction can be written as:

$H^+ + e^- \rightarrow 1/2H_2$ (1.4)

Its standard potential is 0 V vs. NHE and the potential is dependent on pH (E

= 0 V – 0.059(pH) vs NHE). Mechanistically, for the HER in acidic solution, the following possible reaction steps have been suggested.[1.10]

$$H_3O^+ + e^- \rightarrow H_{ads} + H_2O \quad (1.5)$$

$$H_{ads} + H_3O^+ + e^- \rightarrow H_2 + H_2O \quad (1.6)$$

$$H_{ads} + H_{ads} \rightarrow H_2 \quad (1.7)$$

where H_{ads} is the adsorbed hydrogen atom on the surface. Eq. (2.5) is a discharge step (the Volmer reaction), eq. (1.6) is a desorption step (the Heyrovsky reaction), and eq. (1.7) is a recombination step (the Tafel reaction). Therefore, two different pathways for HER can occur. A combination of eq. (1.5) and (1.7) step is known as the Volmer-Tafel mechanism. In this mechanism, protons from the solution are discharged on the surface, forming adsorbed hydrogen atoms. Then, two adjacent adsorbed hydrogen atoms combine to form molecular hydrogen. The combination of eq. (1.5) and (1.6) is known as the Volmer-Heyrovsky mechanism. A proton from the electrolyte solution is discharged on the catalyst surface to form an adsorbed hydrogen atom. This step is followed by combination with another proton and electron to form molecular hydrogen. However, for the reaction to proceed at a sufficient rate, it needs to be catalyzed on an electrode surface. Possible candidates for an HER catalyst include various metals such as Pt, Pd, and Ru as well as metal oxide, carbon, and enzymes with active centers. Using Pt catalyst for HER, equations (1.8) – (1.10) can be described as follows:[1.11]

$Pt + H^+ + e- \rightarrow H\text{-}Pt$ Volmer reaction (1.8)

$2(H\text{-}Pt) \rightarrow H_2 + 2Pt$ Tafel reaction (1.9)

$H\text{-}Pt + H^+ + e- \rightarrow H_2 + Pt$ Heyrovsky reaction (1.10)

HER activity of the catalyst can be characterized by representative parameters; the exchange current density and the bond energy of hydrogen adsorbed to the catalyst.[1.12] During hydrogen evolution, a current I can be described as:[1.13]

$$I = -e(r_+ - r_-) \quad (1.11)$$

where, $r_+ - r_-$ is the net rate of Eq. (1.4). The exchange current is the forward and backward rate when Eq. (1.4) is in equilibrium. The ability of a given metal to catalyze the hydrogen evolution reaction is usually measured by the exchange current density, which is the rate of hydrogen evolution per surface area at the electrode potential when the reaction is at equilibrium. The exchange current density (J_0) is also defined to be the current density at zero overpotential.[1.14] The catalytic effect originates from improving the rate of charge transfer at the interface between the electrode and electrolyte or from lowering the activation energy barrier for a chemical reaction; these catalytic effects are represented by J_0. A higher J_0 indicates that electron transfer or the adsorption/desorption of protons at the electrode/electrolyte can occur more easily with a lower kinetic barrier.

The chemisorption of hydrogen at the catalyst is also an indicator of the ability of catalytic activity for HER. ΔG_{H^*}, the free energy of the adsorbed state is calculated as:[1.13]

$$\Delta G_{H^*} = \Delta E_H + \Delta E_{ZPE} - T\Delta S_H \quad (1.12)$$

where, ΔE_H is the hydrogen chemisorption energy, ΔE_{ZPE} is the difference in zero point energy between the adsorbed and the gas phase, T is the temperature, and the ΔS_H is the entropy of H_2 in the gas phase at standard conditions. The chemisorption energy of hydrogen is also dependent on the surface coverage of the adsorbates. Electrochemical Quartz Crystal Microbalance is useful to find the surface coverage experimentally, and density functional theory calculation can be applied to calculate the chemisorption energy of hydrogen adsorbed on the catalyst, theoretically.

Good catalytic activity requires moderate binding energy between metal catalyst and hydrogen adsorbed for HER. This tendency forms the shape of a volcano. The volcano shape of HER catalysts can be represented by the exchange current density versus the metal – hydrogen bond strength or the exchange current density versus the calculated free energy for hydrogen

adsorption (Figure 1. 1). In Figure 1.1, Pt, Pd, and Ru catalysts are near the top of the volcano curve. Their binding energy to hydrogen is neither strong nor weak. Moderate binding energy gives good catalyst behavior.

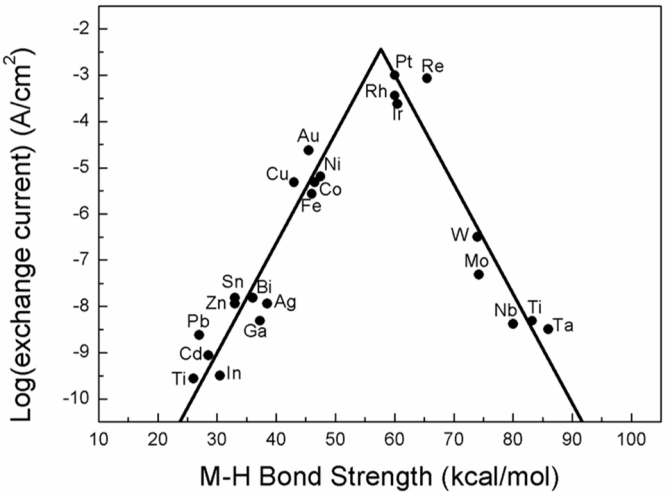

Figure 1.1. Experimentally measured exchange current, log(J_0), for hydrogen evolution over different metal surfaces plotted as a function of the calculated hydrogen chemisorption energy per atom.

The overpotential is the additional energy required to overcome the kinetic barriers inherent to hydrogen evolution reactions at the electrode/electrolyte interface. This overpotential is related to the logarithm of the current density as described by the Tafel law:[1.14]

$$\eta = A \ln (J/J_0) \quad (1.13)$$

where, parameters η is the overpotential, A is the so-called "Tafel slope", J is the current density, J_0 is the so-called "exchange current density". The exchange current density includes the activity of the catalyst on the electrode and Tafel slope indicates the mechanism of the water splitting reaction on the electrode. Examples of Tafel plot are plotted in Figure 1.6 (c), 1.7 (b), and 1.8 (c). The Tafel slope is also defined to be a measure of the potential increase required to increase the resulting current by 1 order of magnitude. The Tafel slope is an inherent property of the catalyst that is determined by the rate-limiting step for HER. The value of the Tafel slope also relates to the adsorbed hydrogen coverage (θ_H) on the surface of the electrode.[1.15] If the recombination of adsorbed hydrogen (the Tafel reaction) is the rate-determining step for the HER and if the coverage is very high ($\theta_H \approx 1$), the measured Tafel slope is below 40 mV/decade. However, if the electrochemical desorption step (the Heyrovsky reaction) is the rate-determining step, a Tafel slope of 40 ~ 118 mV/decade is measured and is dependent on the value of θ_H (0 ~ 1).

1.3 Graphene-based HER electrocatalysts

The design and preparation of carbon-based catalysts is a significant research part for inexpensive, environment-friendly, and durable catalysts that may replace previously developed noble metal catalysts. In particular, graphene possesses extremely high transparency and superior carrier mobility.[1.16] It has been reported that the reduced graphene oxide (rGO) incorporated catalytic materials shown an improved activity in HERs as well as oxygen evolution reactions (OERs) or oxygen reduction reactions (ORRs).[1.17] However, in most cases, previous graphene based electrochemical catalysts have been limited to utilize only electrically conductive substrates or supporters.

Recently, new possibilities have been investigated that monolayer graphene acts as an electrocatalyst for efficient HER. Uk Sim et al., reported that monolayer graphene acts as a catalyst for hydrogen evolution reaction on Si-electrode and boost their catalytic activity by plasma treatment in N_2-ambient.[1.18] Plasma treatment induces the abundant defects and the incorporation of nitrogen atom in graphene structure, which can act as catalytic sites on graphene. Monolayer graphene containing nitrogen impurities exhibits a remarkable increase in the exchange current density and leads to significant anodic shift of the onset current from an Si-electrode. The electro-catalytic activity of the carbon-based catalyst was much lower than other metal-based catalysts, but the HER activity of carbon catalyst has increased gradually. The J_0 of monolayer graphene is also comparable to that of the other non-noble metal catalyst, nanoparticulate MoS_2.[1.19-1.21] J_0 can be accurately calculated by considering the number of active sites. To sum up, while the representative carbon-based catalyst, graphene, has the catalytic activity for HER, the identification and quantification of the active sites of the single monolayer graphene should be further investigated for comparative study.

Furthermore, the origin of HER activity of heteroatom-doped graphene was

investigated, and studies were conducted to examine the design rule for graphene based HER catalyst.[1.22] As shown in Figure 1. 2a, heteroatom, i.e. N, B, P, S, and O substituted graphene were synthesized and heteroatom doped graphene in the various positions were established. Based on this, the density functional theory (DFT), mainly calculated the strength of hydrogen adsorption (intrinsic property), the reaction thermodynamics and the activation barrier, was accurately computated at each active site. As shown in Figure 1. 2b, the Gibbs free energy change for hydrogen adsorption (ΔG_{H^*}) of the various heteroatomic sites was lower than that of the pristine graphene edge sites. The electrochemical properties of the heteroatom doped graphene were measured and the relationship between the tafe slope and the valcano plot related to theoretical i_0 per active site, was shown in figure 1. 2c,d. Thus, this graphene based catalyst activity trend can be compared with actual catalyst activity and calculated values. In addition, the electronic structure was determined using the density of state based descriptor to raise the valcano plot with respect to the physicochemica property. The relationship between hydrogen absorption ability and electronic structure can be explained by the bonding formation shown in figure 1. 3a,b. When the proton in aqueous solution is adsorbed in form of H*, the strength of the adsorbate is related to the anitibonding state (σ*). Therefore, the closer DOS peak of the active site to the Fermi level of carbon, the greater the hydrogen adsorption strength. Through the intrinsic electronic structure and extrinsic physicochemical properties of graphene, they have described the design guidelines for metal-free graphene HER catalysts consequently. Table 1.1 summarizes a selection of experimental values of exchange current for the hydrogen evolution on carbon-based catalysts.

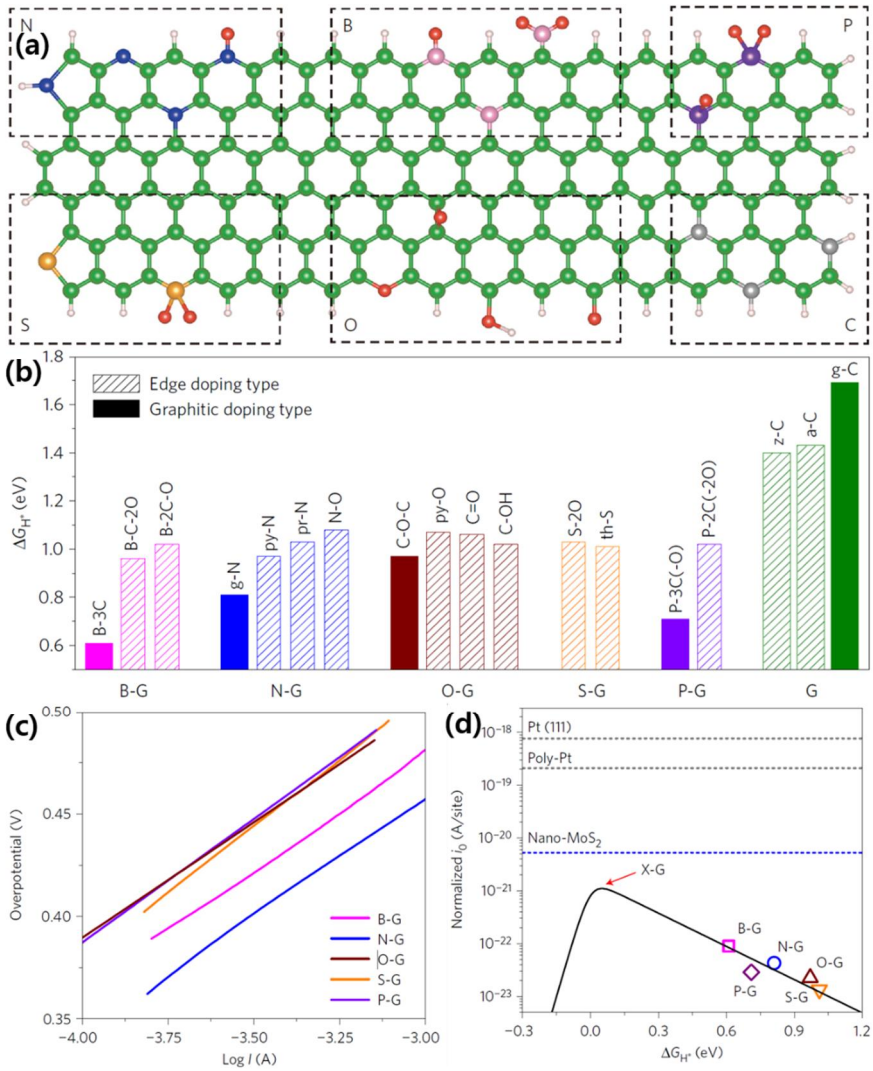

Figure 1. 2. Heteroatom-doped graphene graphitic model and its HER parameter depending on the chemical structure of graphene (a) Schematic illustration of the heteroatom-doping chemical structure. (b) The computed Gibbs free energy for hydrogen adsorption. (c) Tafel slope of different doped-graphene catalyst in 0.5 M H_2SO_4 aqueous solution, (d) Volcano plot between Gibbs free energy for hydrogen adsorption and i_0 to the activity per active site. Reprinted with permission (a-d) from ref. 1.22 Copyright 2016 Macmillan Publishers limited, Nature.

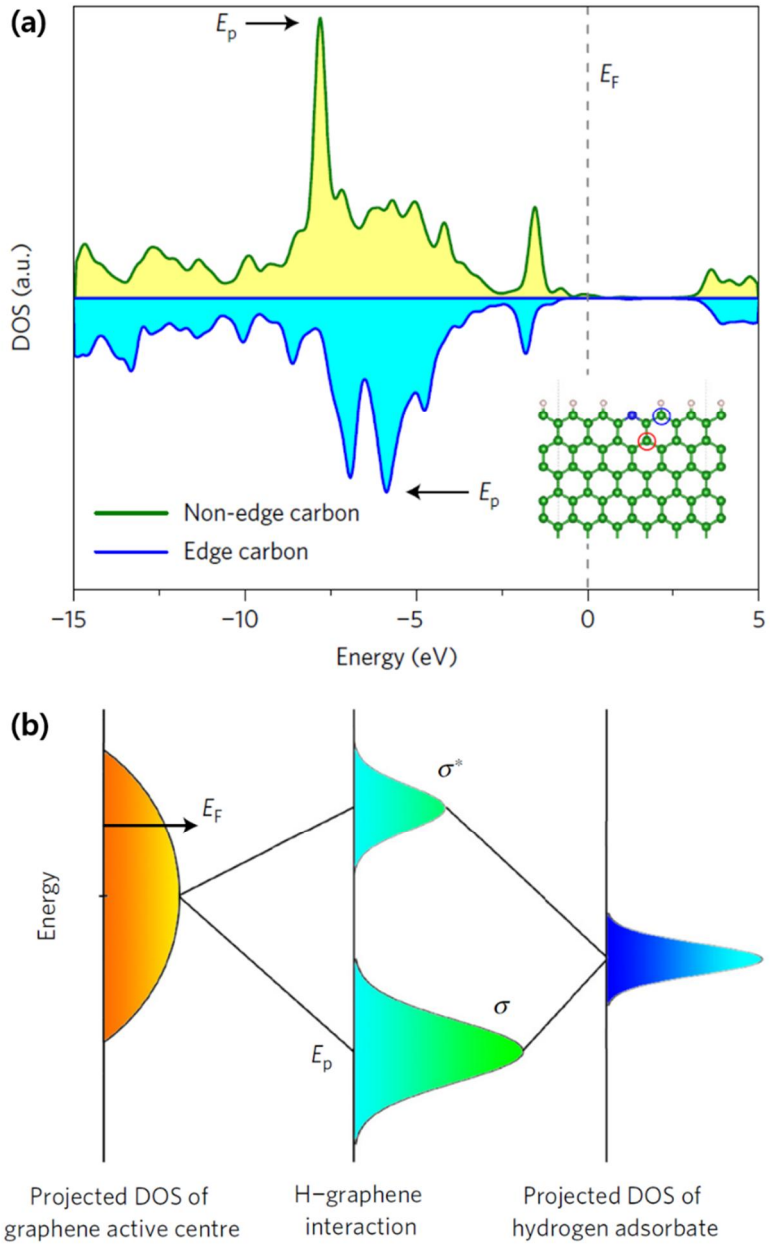

Figure 1. 3. Electronic structure origins of HER performance on graphene based catalyst. Reprinted with permission (a-b) from ref. 1.22 Copyright 2016 Macmillan Publishers limited, Nature.

Catalyst/Substrate (adhesive)	Electrolyte	Activity		Ref. (Year)
		Tafel Slope (mV/dec)	Exchange current $-\log(j_0)$ (A/cm^2)	
Monolayer graphene	1M HClO4	75	7.57	[1.18](2013)
N doped Gr	0.5M H_2SO_4 0.1M KOH	116 143	7.15 9.93	[1.23](2014)
P doped Gr	0.5M H_2SO_4 0.1M KOH	133 159	8.05 10.79	[1.23](2014)
N,P doped Gr	0.5M H_2SO_4 0.1M KOH	91 145	6.62 9.40	[1.23](2014)
B doped Gr	0.5M H_2SO_4	112.3	NA	[1.22](2016)
N doped Gr	0.5M H_2SO_4	115.5	NA	[1.22](2016)
O doped Gr	0.5M H_2SO_4	113.0	NA	[1.22](2016)
S doped Gr	0.5M H_2SO_4	112.8	NA	[1.22](2016)
P-doped Gr	0.5M H_2SO_4	120.6	NA	[1.22](2016)

Table 1.1. Selection of experimental values of Tafel slope and exchange current for the hydrogen evolution on carbon based catalyst system.

1.4 Polydopamine and its derivatives

Synthesis and polymerization mechanism of polydopamine

The observation of natural phenomena can be breakthrough for discovery of novel materials and pathway of innovative renewable energy technology. Recently, Surface modifications offer the protection of materials from external stimulation via reagents such as strong oxidants, acid, or base. Furthermore, modification of the surfaces can control the surface properties and provide new functionalities to them, a feature that is especially important in some critical fields. Among the many biomimetic researches, surface coating process using polydopamine (PDA) which motivated by mussel adhesive protein (MAPs) is suitable examples for this discovery.[1.24] Polydopamine (PDA), which is an eco-friendly, biomimetic mussel adhesive molecule, can be easily synthesized by oxidative polymerization of dopamine under alkaline aqueous condition. This solution oxidative method is commonly used synthetic method for polymerization method of dopamine. By oxidative polymerization of dopamine, DOPA and other catechol compound can covalently (or noncovalently) attached to diverse surface. PDA is also found in main pigment of naturally occurring melanin (eumelanin) and has hetero-aromatic structure with many functional groups such as catechol, o-quinone, amino, and imine group.[1.25] These functional groups impart a potential advantage in a variety of applications, such as the coordination bond with the transition metal ion, the chemical composition of the desired molecule. In addition, these structural features are related with its physicochemical properties. As results, polydopamine exhibits amazing properties found in naturally occurring melanin, such as optical, electrical, and biocompatibility. With these advantages, a poly dopamine can be variously utilized not only the coating material, but also a wide range of applications, for example, chemical, medical, engineering materials, and environmental and energy material.

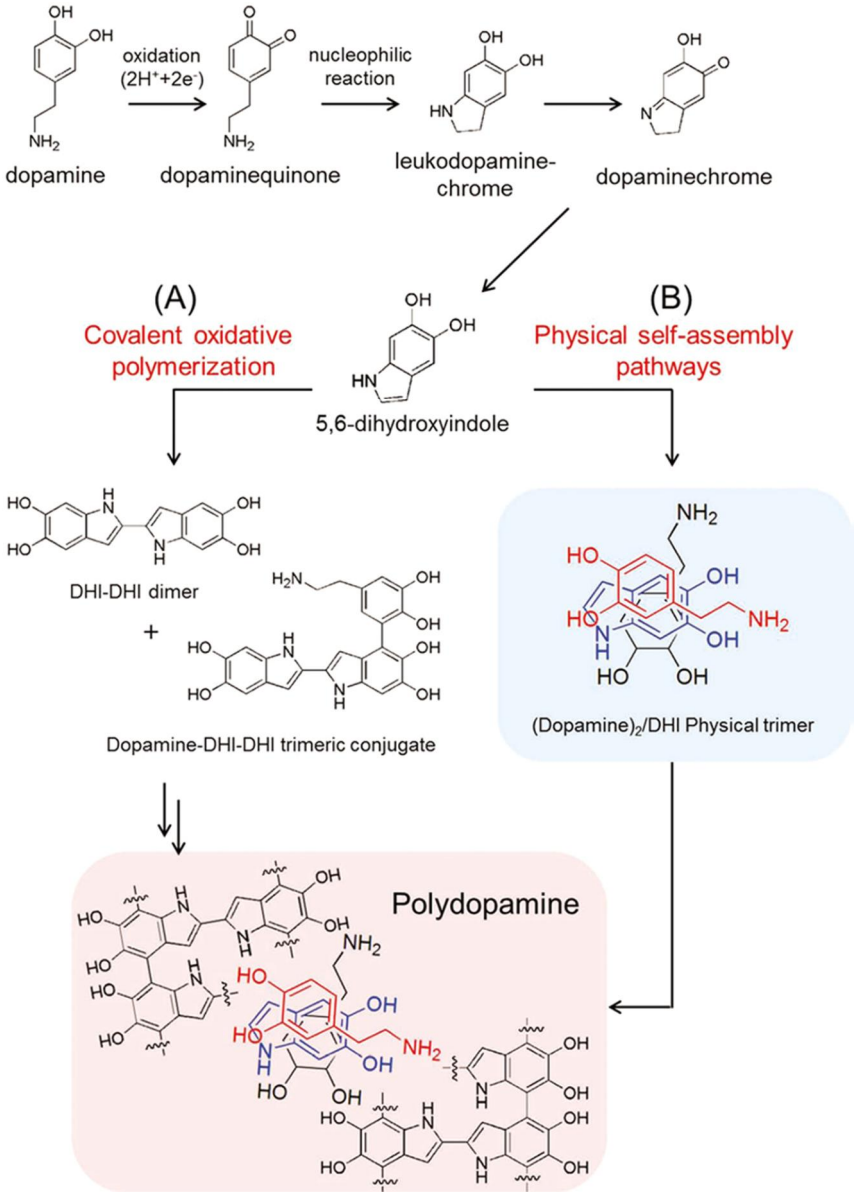

Figure 1. 4 Polymerization mechanism of polydopamine. Reprinted with permission from ref 1.26 Copyright 2012 Wiley-VCH

Adhesive Property

Strong adhesive to all type of organic, inorganic surface is the most important property of polydopamine derivatives.[1.27-1.31] To date, although the catechol group and the primary amine of the poly dopamine is known to play a significant role in the adsorption, the bonding mechanism of a poly dopamine was not exactly understood. Many researchers have studied the mechanisms by looking at the pattern of the poly dopamine adsorbed on a variety of substrate. Based on previous studies[1.32-1.45], the adhesion mechanism of polydodamine consisted of two adhesion mechanisms depending on the substrate: covalent binding and noncovalent binding.

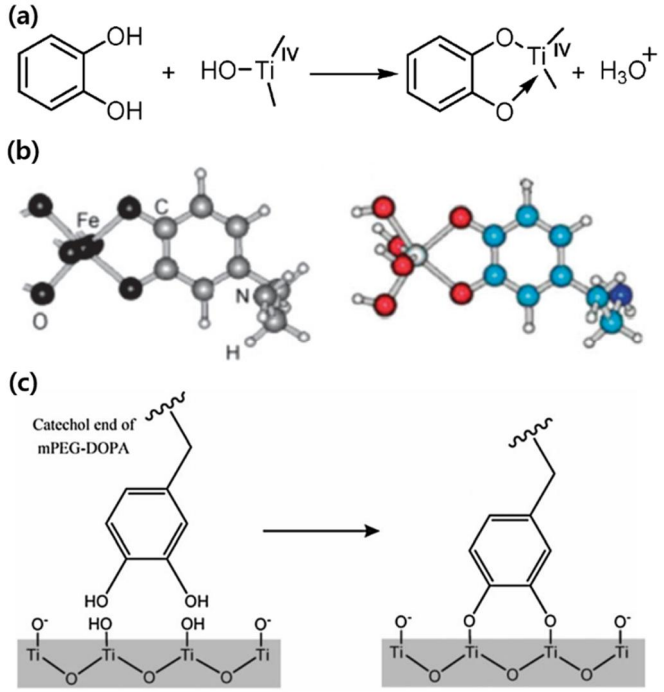

Figure 1. 5. Proposed mechanism of polydopamine adhesition (a) Complexation of the TiO_2 surface via catechol group, (b) Molecular structure of catechol-metal oxide configuration with Fe_2O_3 and TiO_2 nanoparticles. (c) TiO_2-mPEG-DOPA binding mechanism, resulting in depetion of hydroxyl group on surface

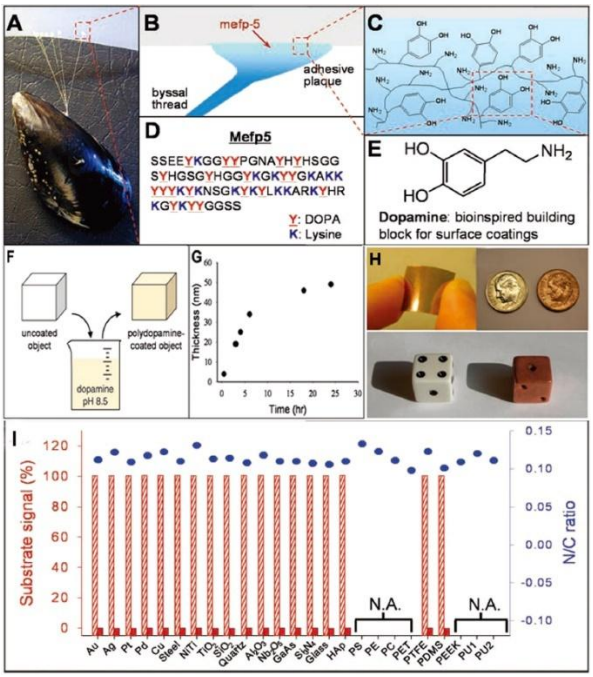

Figure 1. 6 (A-D) Photograph of mussel and amino acid sequence of Mefp-5 in the foot protein. (F) Schematic illustration of deposition process of polydopamine thin film. (G) The thickness of polydopamine film with increasing deposition time. (H) Electroless metallization of polydopamine-coated substrates. (I) XPS spectra of 25 different substrates coated by polydopamine. Reprinted with permission from ref 1.24. Copyright 2007 Science.

Metal ion Chelating and Redox property

Strong coordination ability of catechol group in polydopamine to various multivalent transition metal ions such as Cu^{2+}, Fe^{3+}, Mn^{2+}, Mn^{3+}, Ti^{2+}, Ti^{3+} and Zn^{2+}, etc., is another most attractive chemical property. This coordinating properties are associated with many functional groups of polydopamine, such as o-quinone, primary, secondary and aromatic of amine.[1.46] It is found that the binding configuration appears differently depending on the pH of the solution. For example, binding structure of synthetic, natural melanin with Cu2 + ion were studied through ESR spectra using $^{63}Cu^{2+}$ probe.[1.47-1.48]

(1) Solution pH < 5, the ESR spectra indicate that the the Cu^{2+} ion formed a bidentate bond with the carboxyl group and the nitrogen-carboxyl group of melanin.

(2) Solution pH = neutral pH, the ESR spectra indicates that the Cu^{2+} ions can be formed complexation with the phenolic, hydroxyl group of melanin.

(3) Solution pH >> alkaline condition, Cu^{2+} ions can be complexed to either three or four nitrogen functional group in melanin.

Furthermore, polydopamine can be serve the activity for reduction agent of some noble metal such as Pt, Au and Ag under alkaline condition. It is found that the deposition of Ag has little effect on the ESR signal of the polydodamine film. This phenomenon suggested that oxidation of a certain amount of catechol group into quinone in polydodamine can activate the metal reduction process then finally reduced noble metal.[1.49] These metal chelating and the redox activity properties of this polydodamine attracted considerable interest in the preparation of various organic-inorganic hydrid materials.

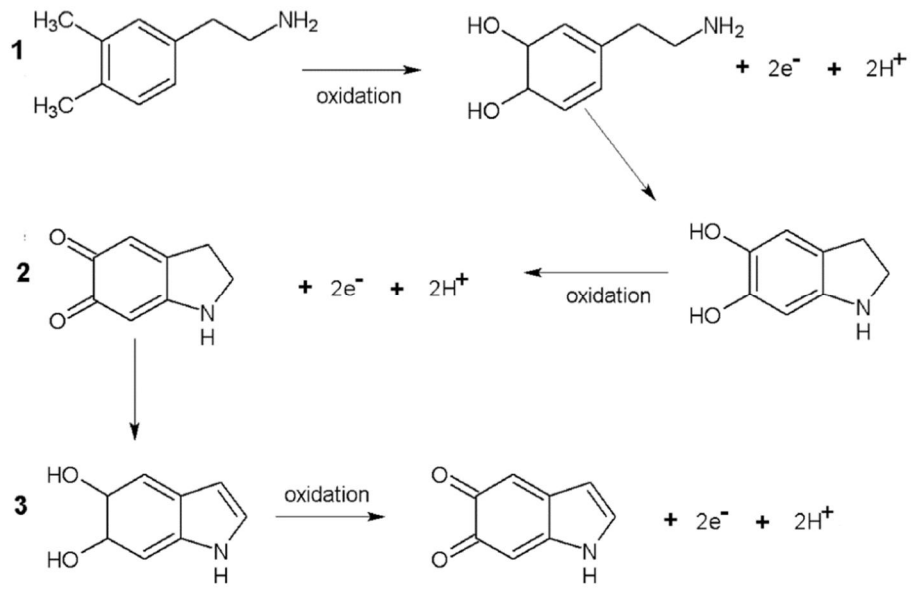

Figure 1. 7. Oxidation step of dopamine in alkaline condition Reprinted with permission from ref 1.50. Copyright 2011 American Chemical Society.

Electronic and protonic conductivity

Melanin is the most common material of pigment in the human body, with diverse functions including uv-protection, antioxidive agent, metal ligand, and free radical elimination. Melanin is also involved in the case of skin cancer and Parkinson's disease. Especially, biologically derived batteries, chemical sensors based on eumelanins and catalysts for organic synthesis have recently been reported. Polydopamine, a melanin-like synthetic macromolecule, is a resourceful platform for biofunctional applications.

Eumelanin is a heterogeneous macromolecule arising in part from the oxidation of L-DOPA via 5,6-dihydroxyindole (DHI). It is made up oligomeric species of DHI, 5,6-dihydroxyindole-2-carboxylic acid (DHICA), and their various chemical structure, namely the ortho-hydroquinone (H2Q), semiquinone (SQ), and (indole)quinone (Q) forms, as well as the tautomer of Q, quinone imine (QI) (Figure 1.7).[1.50] From a structural point of view, eumelanins is significantly similar with polyindole conducting polymers. The structure of macromolecular structures of eumelanin depend on the (bio-)synthetic conditions including on pH, oxidant, and/or metal ion. Several studies show the formation of planar oligomer sheets, which assembled via π–π interaction, convalent bonding and form disklike structure. The electrical, protonic conductivity of eumelanin, demonstrated by a thermally generated, strongly hydration-dependent conductivity, and weak photoconductivity, have attracted researchers even since the 1960s. Electronic band structures of eumelanin in analogy to inorganic semiconductors were proposed based on the strong broad-band UV−vis absorption and the their conjugated, stacked molecular structure. After the study of a reversible resistive switching in eumelanin pellets reported by McGinness et al. in 1974, electrical measurements on pellets and thin films have been suggested within concept of the amorphous semiconductor model. Within this model, the considerable hydration dependence of the conductivity transition has been intepreted by the

increase of the dielectric constant in the presence of water. This increased dielectric constant decreases the activation energy for hopping mechanism of charge carriers. Several studies on eumelanin pellets or thin films also indicated evidence of proton as charge carrier. However, besides the early work of Powell and Rosenberg based on a coulometric measurement, No one could indentify a dominant role to protons for charge transport. Recently, it is found that the previous amorphous semiconductor model cannot properly explain the hydration dependency for conductivity of eumelanin pellets by Mostert et al. They probed the evidence of locally mobile protons and extrinsic free radicals by muon spin relaxation and electron spin resonance measurements and, then concluded that eumelanin is a hybrid protonic-electronic conductor

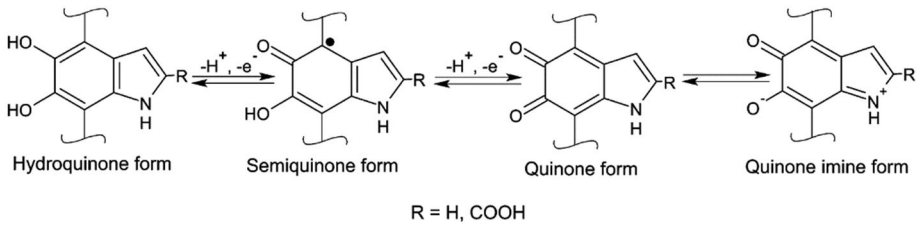

Figure 1. 8. Redox Forms of the final monomer precursors of eumelanin and 5,6-Dihydroxyindole-2-carboxylic acid

Hybrid platforms of polydopamine derivatives

In the view of the characteristic of polydopamine, diverse polydopamine hybrid materials can be prepared and applied as following four ways.

(1) polydopamine itself perform as the passivation layer for serving the interesting properties related to their functional groups including the amine, catechol, and imine, regardless of the type of substrate.
(2) Polydopamine can play a role of reductant and the stabilization agent for the inorganic-organic platform.
(3) Under specific stimuli, Polydopamine can form the particular structures, which can be utilized for diverse application, including sensor, actuators and other bio-applications
(4) Polydopamine can be transform carbon structure via calcination under inert atmosphere.

In the early stages of the study of polydodamine, most have focused on areas that alter the surface properties of certain materials. Through the simple dipping method in a alkaline dopamine solution, the surface properties of various substrates, i.e., metal, metal oxides, and polymer, were modified. In this way, dopamine grafting with DNA, amino acid, PEG polymer, enzyme, metal oxide, graphene, and other molecules are utilized as property converter for preparation of bioactive, chemically reactive layer (Figure 1. 6).

Wang and co-workers fabricated Au nanoparticle sensitive to external pH environment. When an Au precursor is present in a solution in which oxidation of dopamine occurs, polydopamine is synthesized and Au nanoparticles are formed on its surface. At pH 3 or lower, polydopamine-Au janus nanoparticles are formed. It is possible to explain through electrical repulsion characteristic of the pka value of dopamine, which is positively charged at pH 4 or lower, but exhibits repulsion with Au + ion at lower than 2.3. However, at around pH 3, the repulsion force is sharply reduced, and then polydopamine-Au janus nanoparticles are prepared as shown in Fig 1. 9.

In recent years, by using the structural properties of polydopamine, several studies have been conducted on the application of carbon precursor for energy applications. Polydodamine is a macromolecule of aromatic ring structure containing nitrogen, which is transformed into nitrogen-doped carbon by heat treatment under inert gas atmosphere. The inorganic-carbon structure was easily synthesized by heat treatment using polydopamine, which can bind to various transition metals. In addition, graphene or CNT surface, which can be used as a skeleton, was easily bonded to the transition metal by using polydodamine. Using these environmental friendly method, they have shown that polydopamine precursors can be applied to various electrochemical catalysts as well as co-catalyst or/and protecting layer including ORR, OER, and HER catalyst. (Figrue 1.9)[1.51-53] Therefore, it will be possible to synthesize electrochemical catalysts with very high properties in a very easy way.

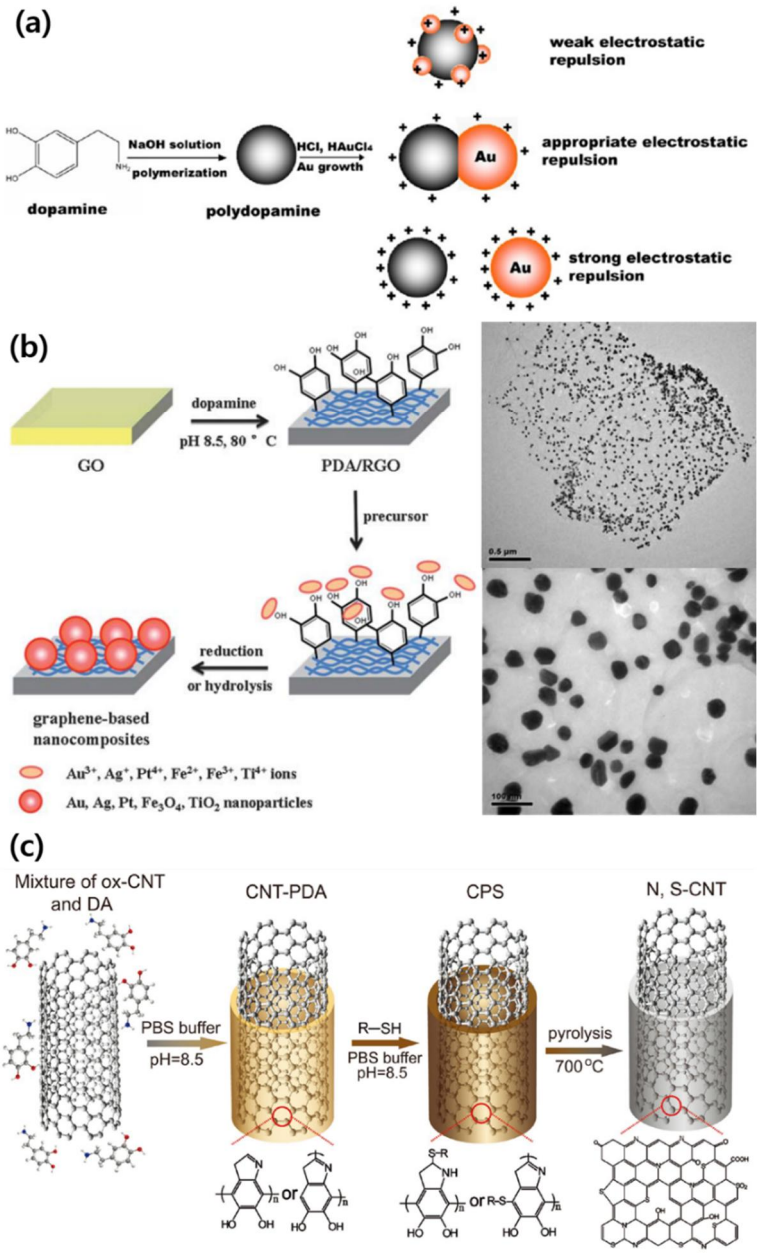

Figure 1. 9. Hybrid Polydopamine derivatives for diverse application (a) Au-polydopamine janus nanoparticle, (b) Prepartion of transition or noble metal /PDA/RGO, (c) N, S Heteroatom doped-CNT for HER, OER dual electrocatalyst.[1.51-1.53]

1.5 Bibliography

1.1. P. M. Cox, R. A. Betts, C. D. Jones, S. A. Spall, I. J. Totterdell, *Nature* 2000, ***408***, 184-187;

1.2. J. R. Petit, J. Jouzel, D. Raynaud, N. I. Barkov, J. M. Barnola, I. Basile, M. Bender, J. Chappellaz, M. Davis, G. Delaygue, M. Delmotte, V. M. Kotlyakov, M. Legrand, V. Y. Lipenkov, C. Lorius, L. Pepin, C. Ritz, E. Saltzman, M. Stievenard, *Nature* 1999, ***399***, 429-436;

1.3. J. L. Sarmiento, C. Le Quéré, *Science* 1996, ***274***, 1346-1350;

1.4. S. Solomon, G.-K. Plattner, R. Knutti, P. Friedlingstein, *Proceedings of the National Academy of Sciences* 2009, ***106***, 1704-1709;

1.5. K. Caldeira, M. R. Rampino, *Geophysical Research Letters* 1991, ***18***, 987-990.

1.6. D. G. Nocera, *Daedalus* 2006, ***135***, 112-115;

1.7. N. S. Lewis, D. G. Nocera, *Proceedings of the National Academy of Sciences* 2006, ***103***, 15729-15735;

1.8. A. J. Esswein, D. G. Nocera, *Chemical reviews* 2007, ***107***, 4022-4047.

1.9. U. S. E. I. Administration., 2013.

1.10. B. E. Conway, B. V. Tilak, Electrochimica Acta 2002, 47, 3571-3594.

1.11. H. Wolfschmidt, O. Paschos, U. Stimming, in Fuel Cell Science, John Wiley & Sons, Inc., 2010, pp. 1-70

1.12. B. E. Conway, G. Jerkiewicz, Electrochimica Acta 2000, 45, 4075-4083.

1.13. J. K. Nørskov, T. Bligaard, A. Logadottir, J. R. Kitchin, J. G. Chen, S. Pandelov, U. Stimming, Journal of The Electrochemical Society 2005, 152, J23-J26.

1.14. J. Tafel, *Z. phys. Chem* **1905**, *50*, 641.

1.15. B. E. Conway, B. V. Tilak, *Electrochimica Acta* **2002**, *47*, 3571-3594.

1.16. K. Novoselov, A. K. Geim, S. Morozov, D. Jiang, M. K. I. Grigorieva,

S. Dubonos, A. Firsov, *Nature* **2005**, *438*, 197-200.

1.17. aY. Liang, Y. Li, H. Wang, J. Zhou, J. Wang, T. Regier, H. Dai, *Nature Mater.* **2011**, *10*, 780-786; bJ.-D. Qiu, G.-C. Wang, R.-P. Liang, X.-H. Xia, H.-W. Yu, *J. Phys. Chem. C* **2011**, *115*, 15639-15645; cQ. Xiang, J. Yu, M. Jaroniec, *Chem. Soc. Rev.* **2012**, *41*, 782-796.

1.18. U. Sim, T.-Y. Yang, J. Moon, J. An, J. Hwang, J.-H. Seo, J. Lee, K. Y. Kim, J. Lee, S. Han, B. H. Hong, K. T. Nam, *Energy Environ. Sci.* **2013**, *6*, 3658-3664.

1.19. T. F. Jaramillo, K. P. Jørgensen, J. Bonde, J. H. Nielsen, S. Horch, I. Chorkendorff, *Science* **2007**, *317*, 100-102.

1.20. U. Sim, T.-Y. Yang, J. Moon, J. An, J. Hwang, J.-H. Seo, J. Lee, K. Y. Kim, J. Lee, S. Han, B. H. Hong, K. T. Nam, *Energy Environ. Sci.* **2013**, *6*, 3658-3664.

1.21. J. Kibsgaard, Z. Chen, B. N. Reinecke and T. F. Jaramillo, *Nat Mater*, **2012**, 11, 963-969.

1.22. Y Jiao, Y. Zheng, K. Davey, S.Z. Qiao, *Nat energy*, **2016**, 1, 16130-16138.

1.23. Y. Zheng, Y. Jiao, L. H. Li, T. Xing, Y. Chen, M. Jaroniec, S. Z. Qiao, *ACS Nano* **2014**, *8*, 5290-5296.

1.24. H. Lee, S. M. Dellatore, W. M. Miller, P. B. Messersmith, *Science* **2007**, 318, 426.

1.25. J. D. Simon, D. N. Peles, *Acc. Chem. Res*. **2010**, 43, 1452.

1.26. S. Hong, Y. S. Na, S. Choi, I. T. Song, W. Y. Kim, H. Lee, *Adv. Funct. Mater.* **2012**, 22, 4711

1.27. W.B. Tsai, C.Y. Chien, H. Thissen, J.Y. Lai, *Acta Biomater.* **2011**, 7, 2518.

1.28. K. J. Coyne, X. X. Qin, J. H. Waite, *Science* **1997**, 277, 1830.

1.29. A. Ooka, R. L. Garrell, *Biopolymers* **2000**, 57, 92.

1.30. B. P. Lee, J. L. Dalsin, P. B. Messersmith, *Biomacromolecules*, **2002**,

3, 1038.

1.31. B. P. Lee, C. Y. Chao, F. N. Nunalee, E. Motan, K. R. Shull, P. B. Messersmith, *Macromolecules* **2006**, 39, 1740.

1.32. Q. Ye, F. Zhou, W. M. Liu, *Chem. Soc. Rev.* **2011**, 40, 4244.

1.33. V. V. Papov, T. V. Diamond, K. Biemann, J. H. Waite, *J. Biol. Chem.* **1995**, 270, 20183.

1.34. J. H. Waite, T. J. Housley, M. L. Tanzer, *Biochemistry,* **1985**, 24, 5010.

1.35. H. Lee, N. F. Scherer, P. B. Messersmith, *Proc. Natl. Acad. Sci. U.S.A.* **2006**, 103, 12999.

1.36. J. Wang, M. N. Tahir, M. Kappl, W. Tremel, N. Metz, M. Barz, P. Theato, H. J. Butt, *Adv. Mater.* **2008**, 20, 3872.

1.37. L. A. Burzio, J. H. Waite, *Biochemistry* **2000**, 39, 11147.

1.38. M. E. Yu, J. Y. Hwang, T. J. Deming, *J. Am. Chem. Soc.* **1999**, 121, 5825.

1.39. T. H. Anderson, J. Yu, A. Estrada, M. U. Hammer, J. H. Waite, J. N. Israelachvili, *Adv. Funct. Mater.* **2010**, 20, 4196.

1.40. J. Moser, S. Punchihewa, P. P. Infelta, M. Gratzel, *Langmuir* **1991**, 7, 3012.

1.41. T. Rajh, L. X. Chen, K. Lukas, T. Liu, M. C. Thurnauer, D. M. Tiede, *J. Phys. Chem. B* **2002**, 106, 10543.

1.42. S. C. Li, L. N. Chu, X. Q. Gong, U. Diebold, *Science* **2010**, 328, 882.

1.43. J. L. Dalsin, L. J. Lin, S. Tosatti,; J. Voros,; M. Textor, P. B. Messersmith, *Langmuir* **2005**, 21, 640.

1.44. C.-Y. Chien, T.-Y. Liu, W.-H. Kuo, M.-J. Wang, W.-B. Tsai, *J. Biomed. Mater. Res., Part A* **2013**, 101A, 740.

1.45. O. Pop-Georgievski, D. Verreault, M.-O. Diesner, V. Proks, S. Heissler, F. Rypáček, P. Koelsch, *Langmuir* **2012**, 28, 14273.

1.46. A. M. d'Ischia, A. Napolitano, P. Pezzella, T. Meredith, *Angew. Chem., Int. Ed.* **2009**, 48, 3914.

1.47. W. Froncisz, T. Sarna, J. S. Hyde, *Arch. Biochem. Biophys.* **1980**, 202, 289.

1.48. T. Sarna, W. Froncisz, J. S. Hyde, *Arch. Biochem. Biophys.* **1980**, 202, 304.

1.49. V. Ball, I. Nguyen, M. Haupt, C. Oehr, C. Arnoult, V. Toniazzo, D. J. Ruch, *Colloid Interface Sci.* **2011**, 364, 359.

1.50. F. Bernsmann, V. Ball, F. Addiego, A. Ponche, M. Michel, J. J. de Almeida Gracio, V. Toniazzo, D. Ruch, *Langmuir,* **2011**, 27, 2819.

1.51. H. Xu, X. Liu, G. Su, B. Zhang, D. Wang, *Langmuir,* **2012**, 28, 13060.

1.52. L. Guo, Q. Liu, G. L. Li, J. B. Shi, J. Y. Liu, T. Wang, G. B. Jiang, *Nanoscale* **2012**, 4, 5864.

1.53. K. Qu, Y. Zheng, Y. Jiao, X. Zhang, S. Dai, and S.-Z. Qiao, *Adv. Energy Mater.* **2017**, 7, 1602068.

Chapter 2. Experimental and Analysis

2.1 Synthesis of catalysts

Synthesis of graphene

A monolayer graphene was grown on Cu foil by chemical vapor deposition (CVD) and was transferred to SiO_2 surface. In the first step of graphene synthesis, a copper foil was put into a quartz reactor in CVD system and then, heated it up to 1000°C with flowing H_2 at 70 mTorr. Additionally, the sample was annealed for 20 min without changing the condition. The gas mixture of H_2 and CH_4 was flowed with rates of 5 and 50 SCCM for 30 min under 8 Torr. Finally, the sample was rapidly cooled down to room temperature with flowing H_2. After growth, in order to remove graphene on one of the sides of Cu foil, graphene on Cu was placed into plasma chamber (SNTEK). The chamber pressure was pumped down to 50 mTorr, O_2 gas was introduced into the chamber by applying a radio-frequency (13.56 MHz) forward power of 100 W for 10 sec. In addition, to make vacancy sites and N-doping graphene on front side of Cu, low density N_2-plasma was produced by applying 10 W power. The N_2 flow rate was 20 SCCM and the working pressure of the chamber was 120 mTorr. Under these conditions, the plasma treatments were performed with various exposure times from 0 to 16 sec of N_2 plasma to test the electrochemical reaction of graphene surface. Finally, poly(methyl methacrylate) (PMMA) was spin-coated on the graphene and then, copper foil was removed in 0.1 M ammonium persulfate solution. After washing with deionized water, the graphene was transferred on Si substrate and then, PMMA was removed in acetone for 30 min.

Synthesis of graphene layers.

For the various stacked graphenes, the graphene with PMMA was floated on deionized water and transferred onto another graphene layer on Cu and

etched/rinsed again. The transfer and etching/rinsing procedures were consecutively performed for up to five layers of graphene. To synthesize the graphene with defects, the monolayer graphene on the back side of the copper was removed using oxygen plasma, and the graphene on the front side of the Cu was treated with argon plasma (10 W RF power, 4 s). The PMMA layer was coated onto this graphene, and the Cu foil was removed. Then, the treated graphene was transferred onto the silicon or used in the stacking process.

Synthesis of carbon-nanosheet

Carbon nanosheet was synthesized using polydopamine chemistry and detailed process was introduced to make active sites for hydrogen evolution reaction. SiO_2/Si target substrate was immersed in tris-(hydroxy-methyl) aminomethane solution (10 mM, pH 8.5) mixed with dopamine (2 mg). Then, polydopamine films were deposited on the surface of the target substrate. The thickness of the film could be controlled as a function of the immersion time. For carbonization, sample were then placed in a tube furnace for thermal treatment at elevated temperatures in a nitrogen atmosphere.

2.2 Electrode preparation

Preparation of Si photocathode

Boron-doped (p-type) single-crystal Si wafers (4 inch diameter, 500 μm thickness, doped to achieve a resistivity of 10~15 Ω·cm, oriented along the (100) plane) were purchased from Namkang Co. Ltd. The wafers were cut into 1 cm^2 pieces and successively cleaned in acetone, 2-propanol and deionized water for 10 min with sonication. To establish an Ohmic contact between copper wire and the unpolished back side of the Si wafer, a gallium-indium eutectic alloy (Ga:In = 75.5:24.5, Kojundo Chemical Laboratory Co. Ltd.) was incorporated, followed by a silver paste. Epoxy was used to insulate and protect the back contact of Si, except for the intended illumination area

(0.25 cm^2) on the front side of the Si. Graphene was transferred onto the Si surface from the Cu foil. PMMA was spin-coated onto the graphene, and the Cu foil was removed using an ammonium persulfate solution. After washing with deionized water, the graphene was transferred onto the Si substrate, and the PMMA was removed after soaking in acetone for 30 min.

2.3 Analysis methods of synthesized catalyst and electrode

Surface Characterization.

Raman spectra were measured at room temperature with a Renishaw spectrometer at 514 nm using an Ar laser. The spot diameter was ~ 2 μm, and a 50x objective lens was used. UPS spectra were recorded using a using a PHI 5000 Versa Probe (ULVAC-PHI) system. The surface morphologies of the graphene films were investigated using AFM (Park system, Xe-100). Images of the graphene layer were obtained via TEM (FEI-CM20) operated at 200 keV.

Scanning Electron Microscope Analysis

The surface morphology and wire length of nanostructured Si were analyzed by Field-Emission Scanning Electron Microscopy (SEM) using SUPRA 55VP model from Carl Zeiss. For cross-sectional view, samples were carefully cut into two pieces with a diamond cutter. In order to avoid the surface charging, Pt was coated by the sputtering method for 200 sec (about 10 nm thickness) using the BAL-TEC/SCD 005 model prior to the SEM analysis.

Reflectance Measurement

Optical reflectance of Si surface was analyzed by UV/Vis/NIR spectrophotometer (Cary 5000, Agilent Technology) using Diffuse Reflectance Mode and Specular Reflectance Mode. Full scan range was 380

to 2300 nm and scan rate was 600 nm min-1. For comparison, the reflectance of planar Si and Si nanowire sample was measured.

2.4 Characterization method for catalytic activity

The electro-catalytic activity of a catalyst can be measured with cyclic voltammetry (CV) using a rotating disk electrode (RDE). An RDE is a convective electrode system to which the hydrodynamic equations and the convective-diffusion equation have been applied. Using a hydrodynamic working electrode system of RDE, methods involving convective mass transport of reactants and products can be studied. Representative parameters for RDE measurement are the rotating speed, the scan rate, and the applied potential range. To fabricate the working electrode, the catalyst can be loaded on a standard working electrode such as a glassy carbon electrode or a highly ordered pyrolytic graphite (HOPG) that are conductive and inert in an aqueous solution. To load the catalyst on the electrode, several loading methods such as catalyst ink are used. The catalyst powder mixed with a few wt% of Nafion or with a carbon black can be synthesized, loaded on the electrode, and stored at 100 ~ 110 ^{o}C for drying. Glassy carbon is a form of carbon which has been used as an indicator electrode and is a gas-impermeable, electrically conductive material which is highly resistant to chemical attack. In *J-E* curves of the RDE measurements, the current density from the electrolysis of water increases exponentially after onset as the potential is swept from lower to higher cathodic potential. The measured potentials are corrected for the ohmic potential drop (iR) losses that originated from the resistance of the interface between the substrate and the electrolyte. To compare the onset potential for the HER in the RDE system, the potential to attain 0 mA/cm^2 or below -1 mA/cm^2 of HER current density is not usually chosen as the indicating potential because non-faradaic current or background current induced by solid electrodes are generated in the range of low applied

potential. The non-faradaic current or background current may occur due to impurities in the electrolyte or may arise from the double-layer charging process. To compare the catalytic activity for HER, the potential to attain -5 mA/cm^2 of HER current density of bare electrode and of catalyst loaded electrode can be chosen as the onset potential for comparison.

Electrochemical measurements are performed in a three-electrode cell (the working electrode, the counter electrode, and the reference electrode) using an electrochemical analyzer. Pt electrode or HOPG electrode is used for counter electrode and Ag/AgCl/KCl electrode or Saturated Calomel electrode is used as the reference electrode. The reference electrode should be carefully calibrated with respect to the reversible hydrogen electrode (RHE) in an aqueous solution with high purity H_2 saturation at room temperature. The RHE is calibrated to between -0.197 V and -0.266 V vs. the Ag/AgCl/KCl reference electrode as the concentration of KCl varies in the electrode. Since the potential difference between Ag/AgCl and RHE is also dependent on electrolyte pH, temperature, etc, the potential should be carefully measured before each set of measurements and the measurement should be conducted at least several times for each condition.

Electrochemical measurements

Electrochemical measurements were performed in a three-electrode cell using a electrochemical analyzer (CHI 760E, CH Instruments, Inc.). Pt foil or Pt wire was used for counter electrode and Ag/AgCl/3 M NaCl electrode was used as the reference electrode. The reference electrode was carefully calibrated with respect to RHE in an aqueous 1 M perchloric acid solution with high purity H_2 saturation at 25 °C. The RHE was calibrated to between -0.201 V and -0.203 V vs. the Ag/AgCl reference electrode. For the electrochemical study, the Rotating Disk Electrode (RDE) system was purchased from PINE, Inc., and a glass carbon tip was used for the RDE

measurements (dia. 5 mm). For comparison, 10 uL of Pt catalyst ink mixed with 5 wt% Nafion was loaded onto the GC and dried at 110oC. RDE measurements were performed at a differenct rotation speed (500 rpm, 1000 rpm, 1500 rpm, 2000 rpm, and 2500 rpm) and at a differenct scan rate (1 mV/sec, 10 mV/sec, 20 mV/sec, 50 mV/sec, and 100 mV/sec), respectively.

PEC measurements

A 300 W Xe lamp (Oriel) with a water filter was used as a light source with an Air Mass 1.5 Global glass filter (Newport Co., model #81094). During the photocurrent measurements, the light intensity was carefully maintained at 100 mW/cm2 using an optical power meter (Newport, Model 1916-R). PEC measurements were performed in a three-electrode cell using an electrochemical analyzer (CHI 760E, CH Instruments, Inc.). To minimize the hydrogen bubbles adhering to the planar Si surface, the electrolyte was stirred during the measurements without the introduction of an additional surfactant. Pt wire was used as the counter electrode, and an Ag/AgCl/3 M KCl electrode was used as the reference electrode. The reference electrode was carefully calibrated with respect to RHE at 25°C in a 1 M perchloric acid aqueous solution saturated with high-purity H_2. The RHE was calibrated to -0.201 V vs. the Ag/AgCl reference electrode.

Electrochemical AC impedance spectroscopy measurement

Electrochemical AC impedance spectroscopy (EIS) was performed at 0 V vs. RHE under an illumination intensity of 100 mW/cm^2 with a frequency range of 1~10^6 Hz and an amplitude of 5 mV in a three-electrode cell. From the Nyquist plot, an equivalent circuit was designed to analyze the EIS spectra.

Chapter 3. Graphene quantum sheets as HER catalyst from monolayer graphene via nitrogen plasma

3.1 Introducation

Graphene quantum dots (GQDs) exhibit great potential for various optoelectronic applications due to their size-dependent and edge-sensitive photoluminescence properties. Previously, GQDs were mainly synthesized from graphene oxides by chemical exfoliation under strongly acidic environment or by multi-step lithographic methods including masking, patterning and lift-off, which hindered the effi cient preparation of high-quality GQDs for practical applications. On the other hand, nitrogen-functionalization or doping is known to be very helpful to tailor the intrinsic properties of GQDs, but it needs further complicated wet-chemical reactions. Atom-thick GQDs can be called graphene quantum sheets (GQSs), which is expected to show stronger quantum effects derived from monolayer graphene, compared to GQDs obtained from graphene oxides (GOs) or carbon fibers.

Here we report a very simple solvent-free method to prepare nitrogen doped graphene quantum sheets (N-GQSs) by directly applying nitrogen plasma to as-grown graphene on Cu. The resulting N-GQSs can be transferred as a fi lm-like layer or easily dispersed in an organic solvent to be transferred on arbitrary substrates. We also demonstrate that a porous Si-cathode decorated with N-GQSs exhibits enhanced photochemical and electrochemical activities advantageous for solar-driven hydrogen evolution reaction. Thus, it is expected that the N-GQSs converted from monolayer graphene would be useful for a wide range of optoelectronic, electrochemical, and energy storage applications in the future.

Recently, GQD has been attracting much attention in bioimaging, light-

emitting, and photovoltaic applications[3.1-3.3] due to its unique optical properties depending on size and functional edge as well as the accessibility to solution chemistry.[3.4-3.6] This has stimulated tremendous efforts to develop various synthesizing methods such as hydrothermal cutting,[3.7] patterning by nanolithography,[3.8] and electrochemical scissoring of graphene sheets,[3.9] as well as bottom up synthesis by wet chemistry to produce GQDs with different sizes and functionalities.[3.10] Usually, these methods require strongly acidic environment or time-consuming multi-step processes, which is a drawback for more efficient synthesis of high-quality GQDs. Moreover, In order to be used for various optoelectronic and energy applications, GQDs often need to be fabricated as a thin-fi lm structure on a solid interface. However, the GQDs in aqueous solvent are hardly processible because they are unstable in aqueous environment. In addition, preparing GQD fi lms from aqueous dispersion is challenging because spincoating or drop-casting method doesn't provide enough control over thickness and uniformity as well as it requires rigid and flat surface rather than fl exible or conformal substrates.

Plasma treatment is one of the facile ways to tune the intrinsic properties of graphene, and previously, oxygen plasma was applied to prepare chemically functionalized graphene showing uniform photoluminescence and Raman spectral changes originated from its defective structures.[3.10-3.11] On the other hand, chemical doping is an effective way to tune the optical, chemical, and electronic properties of graphene.[3.12] Likewise, the band-gap of GQDs can be engineered by changing size, shape, edge-, and surface functionalities,[3.6,3.13,3.14] leading to tunable photoluminescence with higher intensity. In particular, the functional modifi cation with nitrogen could offer more active sites needed for higher catalytic activities, which is important for various energy applications.[3.9]

Herein, we introduce a simple one-step method to prepare large-scale N-doped GQSs by directly applying nitrogen plasma to as-grown graphene on

Cu, which can be transferred as a film like layer or easily dispersed in an organic solvent. Moreover, we confirm that the N-GQSs transferred on fl at Si and porous Si can be a good photoelectrochemical catalyst for hydrogen evolution reaction (HER). Atomic force microscopy (AFM) and transmission electron microscopy (TEM) images show that the average size of N-GQSs is 4.84 nm, and the substitution of carbon with nitrogen is evidenced by Raman spectroscopy and X-ray photoelectron spectroscopy (XPS). The unique optical properties of N-GQSs were confi rmed by absorption and photoluminescence spectra, showing strong emission with the maximum wavelength of 430 nm when excited by 365 nm radiation source (Xe lamp).

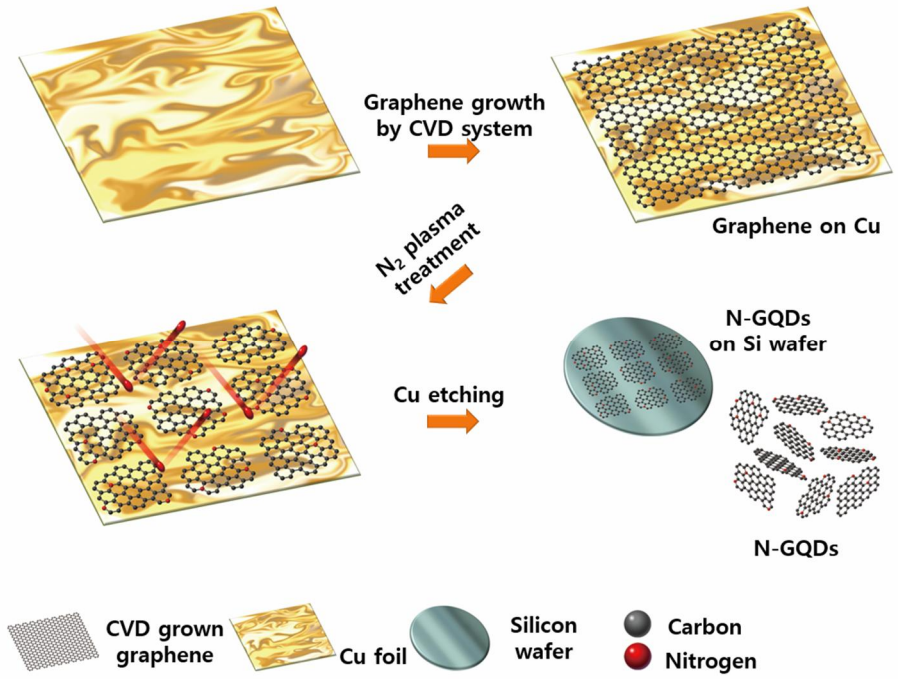

Figure 3. 1. Schematic illustration of the process for N-GQDs

3.2 Results and Discussion

the monolayer graphene was synthesized by using 10 × 10 cm^2 Cu foils as catalytic substrates in 1000 °C quartz reactor with fl owing 50 sccm CH 4 and 5 sccm H 2 for 30 min under 8 Torr. Next, the N-GQSs were prepared by irradiating nitrogen plasma (10 W RF power under 120 mTorr) to as-grown CVD graphene on Cu as shown in Figure 3. 1. Finally, the N-GQSs were transferred using conventional polymer-assisted dry-transfer methods on a target substrate after removing Cu by 0.1 M aqueous ammonium persulphate etchant.[3.15] Alternatively, the fl oating N-GQSs after removing Cu without PMMA can be dispersed into common organic solvent such as dichloromethane using solvent extraction techniques. The AFM images in Figure 3. 2 a-d show the gradual increase of surface roughness with increasing nitrogen plasma treatment time, indicating that the as-grown graphene on Cu is directly converted N-GQSs. The AFM height profi le of N 2 -plasma treated graphene for 16 sec shows the average height of 1.64 ± 0.06 nm. Figure 3. 3 a-b show the N-GQSs fi lm directly transferred from Cu to a SiO 2 substrate after coating with poly(methyl methacrylate) (PMMA) layer. The PMMA can be easily removable by acetone. Figure 3. 3 c-d show the N-GQDs drop-cased onto a SiO_2 substrate from the suspension in dichloromethane. The atomic structures of N-GQSs were investigated by high-resolution transmission electron microscopy as shown in Figure. 3. 3e-g. The sample was prepared by drop-drying the N-GQSs solution on a graphene-supported TEM grid.[3.16] Most of N-GQSs show a size distribution from 3 to 7 nm with an average value of 4.84 nm (Figure 3. 3 h). The clear atomic lattice structure shown in Figure 3. 3 g indicates that the N-GQSs are highly crystalline. After exposure to nitrogen plasma, the D peaks related structural defects at the edges of graphene were signifi cantly increased in Raman spectra (Figure 3. 4a).[3.17-3.18] On the other hand, the shift of D and 2D peaks indicates that the graphene is doped with nitrogen atoms.[3.19]

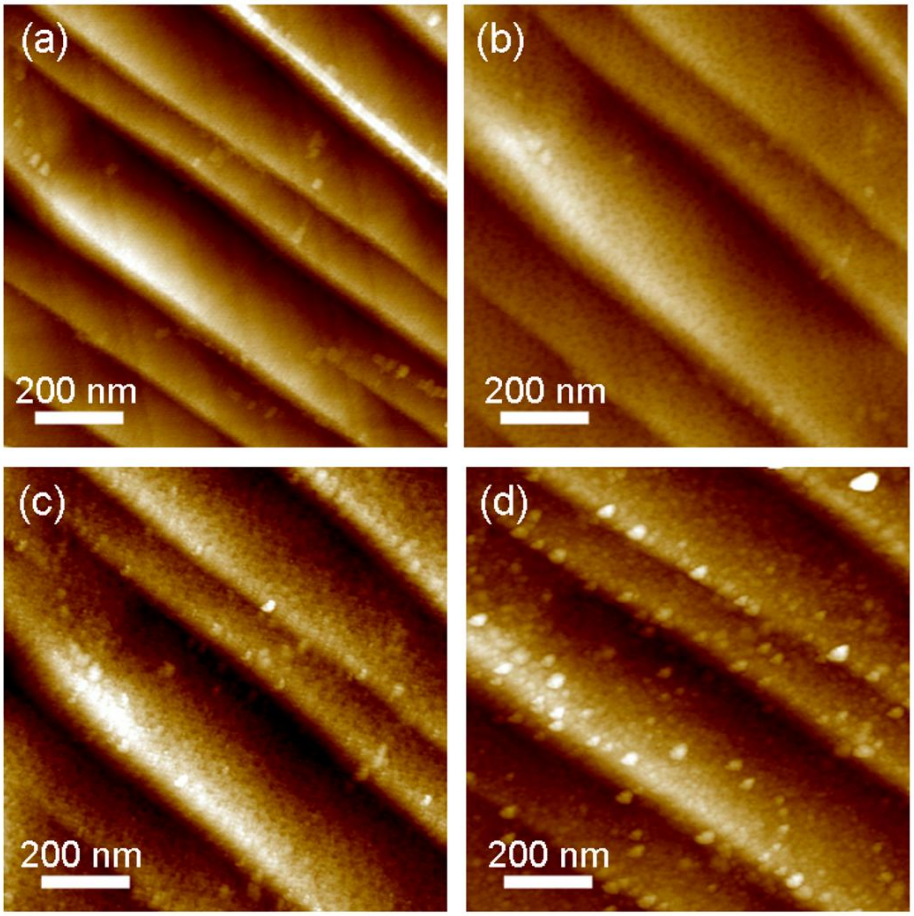

Figure 3. 2. (a)-(d) Surface transition of AFM images of graphene on Cu foil after N_2 plasma treatment for 0, 2, 4, and 6 sec, respectively. The AFM images were obtained form a same position.

X-ray photoelectron spectroscopy (XPS) measurements were performed to determine the chemical composition of N-GQSs (Figure 3.53 b-d). No N 1s peak was observed in monolayer graphene. The strong C 1s peak at 284.8 eV corresponding to sp2 carbon indicates that the conjugated honeycomb lattices are mostly maintained after N_2-plasma treatment. We suppose that the oxygenrelated sub peaks such as C-O (286.6 eV), C=O (288.3 eV), and O-C=O (289 eV) are originated from the reaction of unstable N-GQS edges or defects with oxygen when exposed to air. The C-N bond peak at 285.2 eV in C 1s spectrum (Figure 3. 5c) as well as the pridinic (398.5 eV) and pyrrolic (399.9 eV) peaks in N 1s spectrum (Figure 3. 5d) indicate that nitrogen-to-carbon ratio is ~2.7%. The UV-vis absorption spectrum of the N-GQSs shows an absorption band with a peak maximum (λ_{max}) at 270 nm (Figure 3. 5e). The PL spectrum exited at 370 nm shows a strong peak at λ max = 430 nm. Thus, the N-GQDs emitted intense blue luminescence under 365 nm wavelength irradiation by UV lamp (Figure 3. 5e, inset). We found that the λ max in PL spectra is almost invariable with varying excitation wavelength from 360 nm to 420 nm.

Recently, graphene based-catalyst becomes an attractive candidate for photoelectrochemical reaction.[3.20-3.21] Figure 3. 6 demonstrates the catalyst application of N-GQSs on a fl at bare Si and a porous Si substrates for hydrogen production. The scanning electron microscopy (SEM) images in Figure 3. 6a-b show the cross section of a bare Si and a porous Si and each inset shows the top-view of the sample. To evaluate the photocathodic behavior, N-GQSs were loaded on a bare Si with the dry transfer and on a porous Si with the solution drop-casting. The photocurrent density was measured as potential sweep from 0.4 V to –0.8 V vs. Reversible Hydrogen Electrode (RHE) in a three electrode cell. A light source of a 300 W Xe lamp (100 mW cm^{-2}) with an Air Mass 1.5 Global condition fi lter was illuminated on the samples in an aqueous 1 M perchloric acid solution (pH 0) (Figure 3. 6).

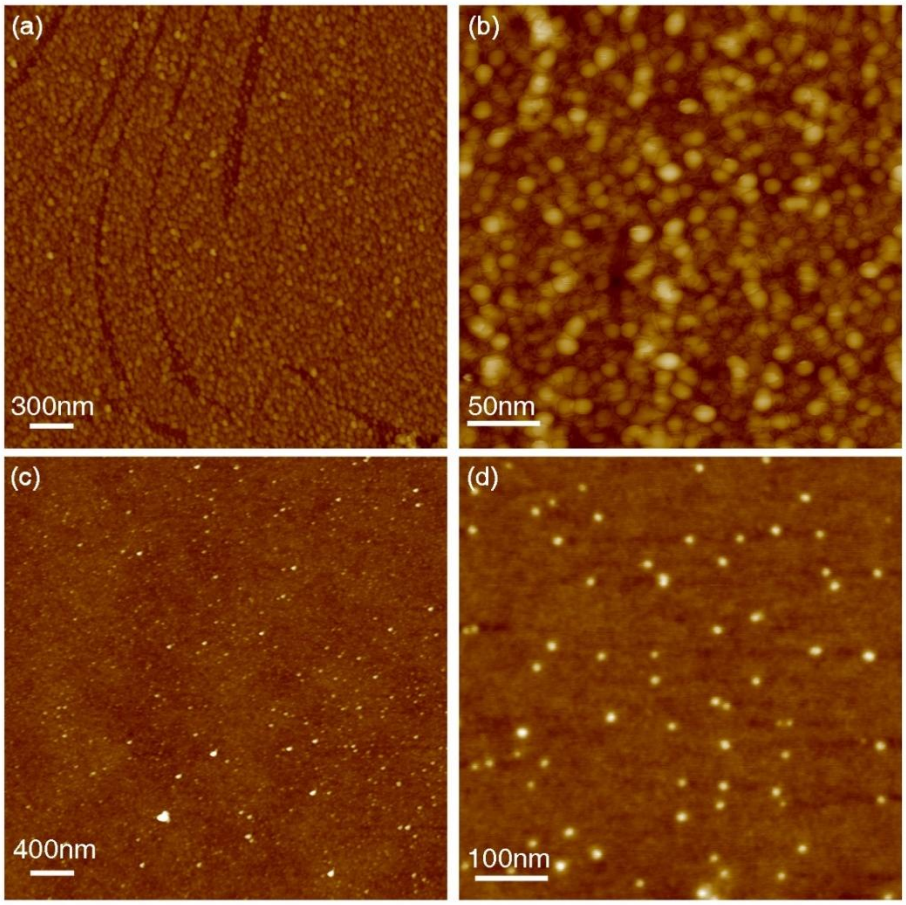

Figure 3. 3. (a), (b) AFM images of the N-GQSs transferred to a SiO_2 substrate using PMMA layer. (c), (d) AFM images of N-GQSs drop-casted from organic solution to a SiO_2 substrate.

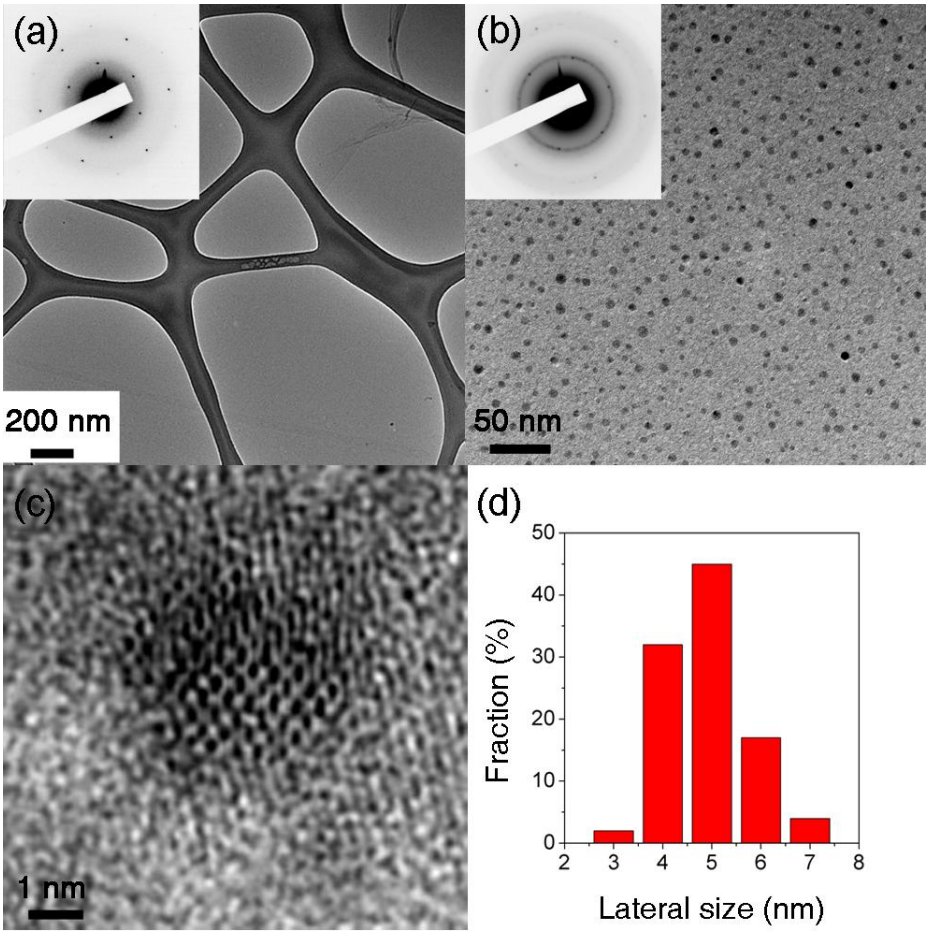

Figure 3. 4. (a) TEM images of monolayer graphene supported by holely carbon grides. (b, c) Low and high-resolution TEM images of N-GQSs on a graphene supported grid. (d) Histogram showing the size distribution of N-GQSs. The insets in e and f show selected area diffraction patterns (SAED) of graphene and N-GQSs.

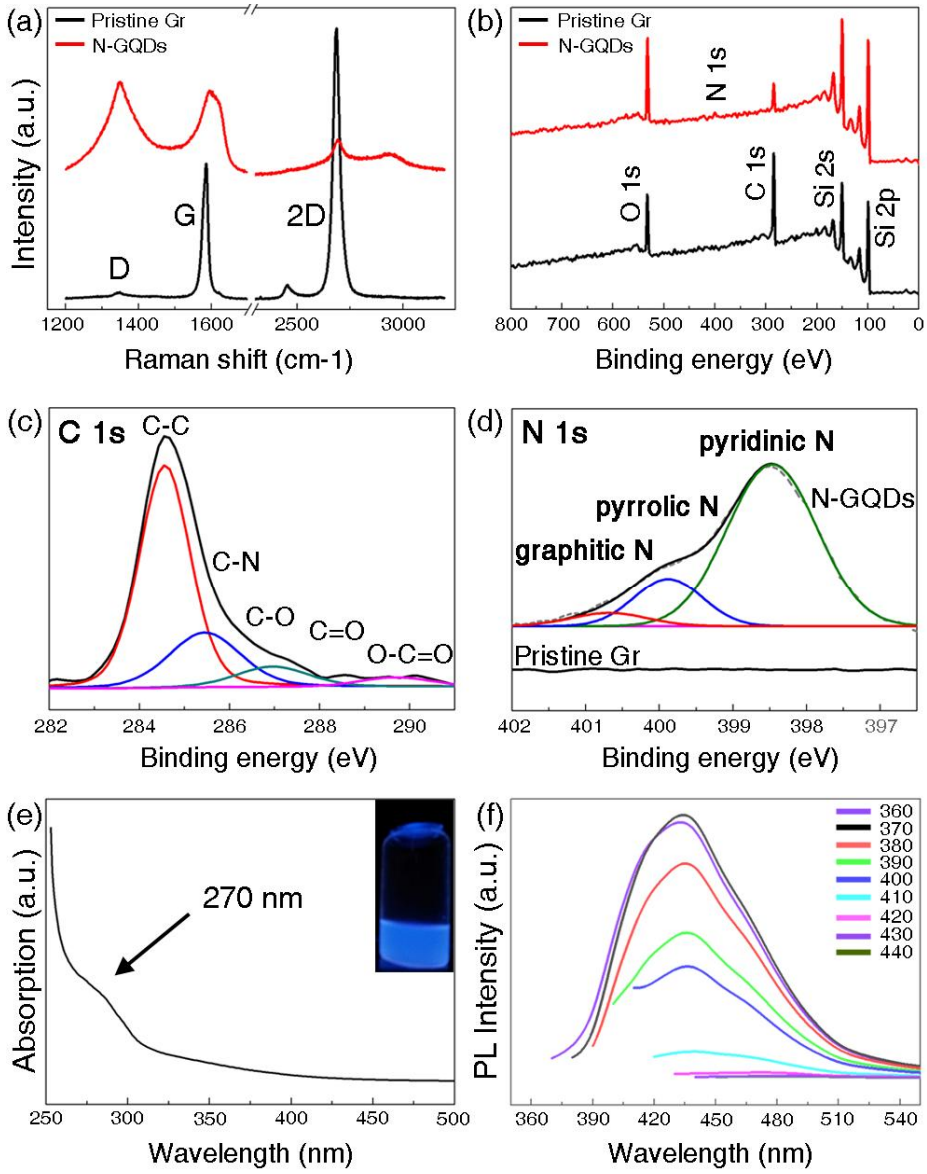

Figure 3. 5. (a) Raman spectra and (b) XPS spectra of as-grown graphene and N-GQSs. (c, d) Detailed C 1s and N 1s XPS peaks of N-GQSs. (e) UV-vis absorption spectra of N-GQSs in dichloromethane. The inset shows a photograph of the N-GQSs solution under 365 nm wavelength UV lamp. (f) Photoluminescence (PL) spectra of the N-GQSs for different excitation wavelengths (360～440 nm).

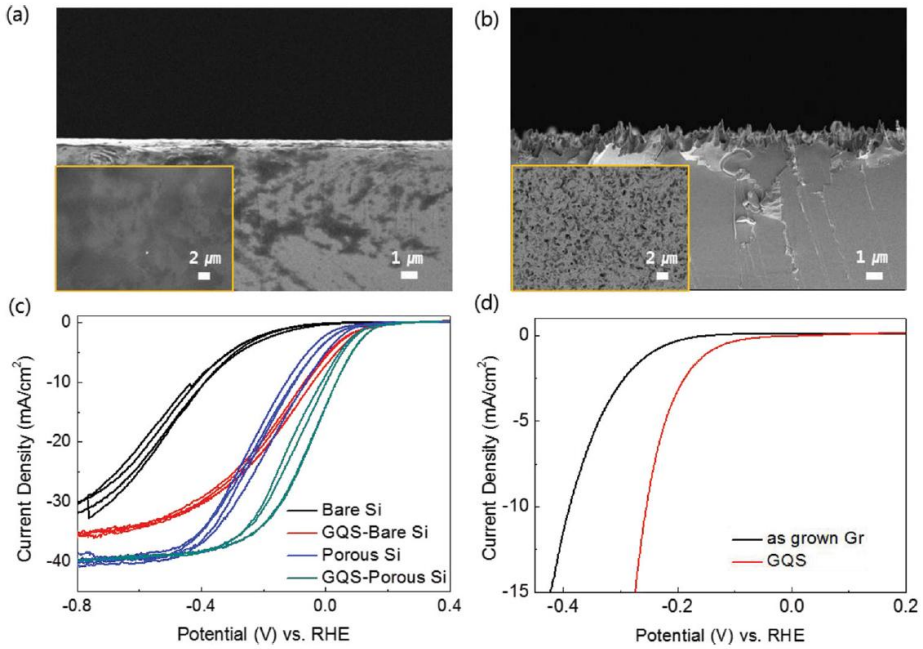

Figure 3. 6. SEM images of (a) bare Si and (b) porous Si. Cyclic Voltammetry (CV) of N-GQSs on bare Si and porous Si. (c) Photocurrent density-potential (J–E) curves for the lightly boron doped p-Si and p-porous Si electrode deposited with N-GQSs.N-GQS s were introduced by dry transfer on bare Si and by wet transferred on porous Si. Each CV process was performed at a scan rate of 0.005 Vs^{-1} . (d) Electrochemical activity of N-GQSs on a Glassy Carbon (GC) electrode with rotating ring disk system. CV data were corrected by current-resistance (iR) compensation.

Interestingly, the N-GQSs exhibit the superior catalytic activity for HER. As shown in Figure 3.6c, the photocurrent density-potential (J–E) curve of N-GQSs/bare Si dramatically is shifted approximately ~0.35 V toward positive potential compared to that of the bare Si as well as the onset potential of N-GQSs also positively shifted by 0.29 V (Table 3.1). Compared to bare Si, porous Si exhibits enhanced limiting current density and positive shift of onset potential ascribed to light trapping effect. In N-GQSs on a porous Si substrate, the positive shift in 0.09 V of the onset potential also shows higher activity for HER compared to that of a porous Si. Figure 3.6d shows the electrocatalytic activity of N-GQSs, CV curves of the samples were obtained without illumination with rotating disk electrode (RDE) system. For the working electrode, N-GQSs were transferred to a glassy carbon tip which is inert in aqueous solution. The J–E curves were swept from 0.1 V to –0.35 V and the onset potential were obtained –5 mA cm^{-2} of HER current density of as-grown graphene and N-GQSs (Table 3.1). The onset potential of N-GQSs is –0.22 V with respect to RHE, which has positive shift by 0.07 V compared to that of as-grown graphene. This result is similar to the photoelectrochemical behavior of the J–E curves, a positive shift in the overall J–E curve induced by N-GQSs. From the above results, we conclude that the N-GQSs show the superior electrocatalytic effect for hydrogen production when combined with Si photocathodes with arbitrary morphologies.

3.3 Conclusion

we have demonstrated the formation of N-doped GQSs from as-grown monolayer graphene on Cu using nitrogen plasma. Various spectroscopic analyses including AFM, TEM, XPS, Raman, and PL indicate the direct formation of high-quality N-GQSs from CVD graphene. The N-GQSs can be transferred onto an arbitrarily shaped photocathode surface to enhance the catalytic activity for photoelectrochemical hydrogen evolution, which would be also useful for various display, energy, and biological applications.

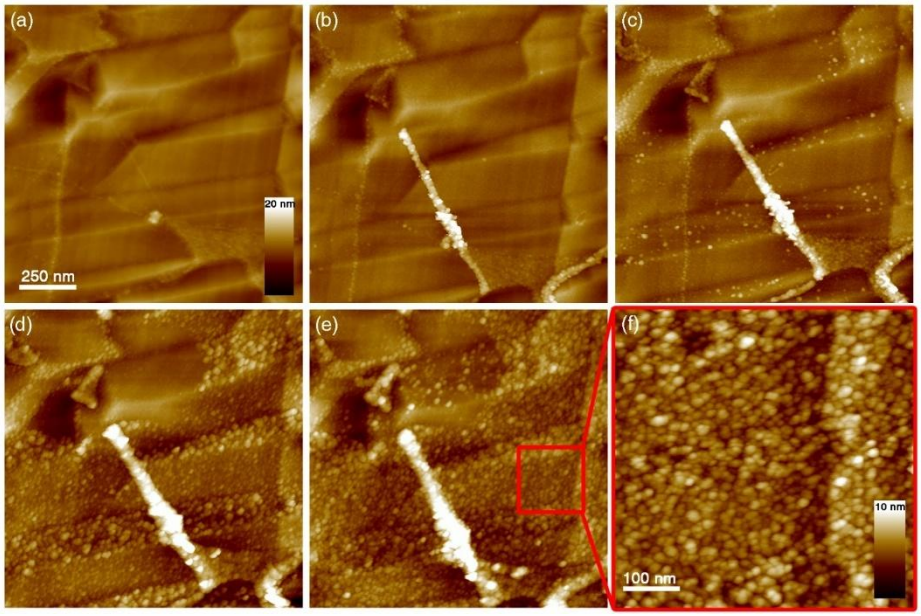

Figure 3. 7. Surface transition of graphene into GQSs on Cu surface as function of time.

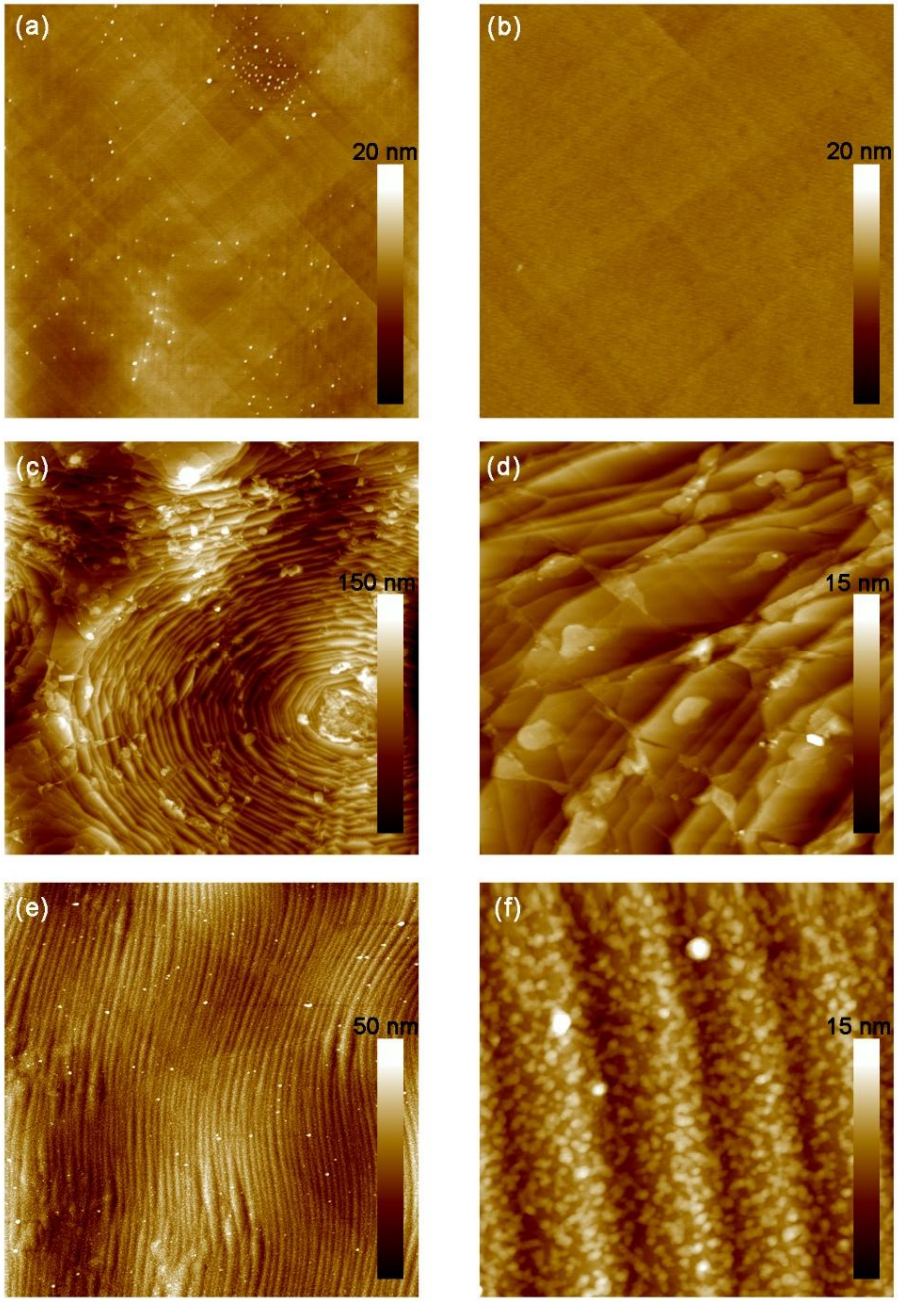

Figure 3. 8. (a-b) AFM images of Cu foil annealed at 1000 °C. (c-d) Monolayer graphene film grown on Cu by CVD. (e-f) N-GQSs via Plasma treatment on Cu.

Table 3. 1. Summary of the experimental data for Si, porous Si and glassy carbon (GC) RDE system

Condition	Electrode	Onset potential [E (V) at -1 mA/cm^2]	E (V) at -5 mA/cm^2
Under illumination (p type Si)	Planar Si	-0.17	-0.29
	Porous Si	0.07	-0.03
	N-GQSs/ planar Si	0.12	0.01
	N-GQSs/ Porous Si	0.16	0.08
RDE analysis	Graphene/ GC	-0.21	-0.29
	N-GQSs/ GC	-0.08	-0.22
	Pt/GC	-0.02	-0.04

Bibliography

3.1. X. Geng , L. Niu , Z. Xing , R. Song , G. Liu , M. Sun , G. Cheng , H. Zhong , Z. Liu , Z. Zhang , L. Sun , H. Xu , L. Lu , L. Liu , *Adv. Mater.* **2010**, 22 , 638 .

3.2. D. I Son , B. W. Kwon , D. H. Park , W. Seo , Y. Yi , B. Adgadi , C. Lee , W. K. Choi , *Nature Nanotech* . **2012** , 7 , 465 .

3.3. a) J. K. Kim , M. J. Park , S J. Kim , D. H. Wang , S.-P. Cho , S. Bae , J. H. park , B. H. Hong , *Acs Nano* **2013** , 7 , 7207 ; b) X. Yan , X. Cui , B. Li , L. Li , *Nano Letters*, **2010** , 10 , 1869 .

3.4. S. Kim , S. W. Hwang , M. Kim , D. Y. Shin , D. H. Shin , C. O. Kim , S. B. Yang , J. H. Park , E. Hwang , S. Choi , G. Ko , S. Sim , C. Sone , H. J. Choi , S. Bae , B. H. Hong , *Acs Nano,* **2012** , 6 , 8203 .

3.5. S. H. Jin , D. H. Kim , G. H. Jun , S. H. Hong , S. Jeon , *Acs Nano* **2013** , 7 , 1239 .

3.6. X. Yan , X. Cui , L. Li , *J. Am. Chem. Soc.* **2010**, 132 , 5944 .

3.7. D. Pan , J. Zhang , Z. Li , M. Wu , *Adv. Mat.,* **2010**, 22 , 734 .

3.8. J. Lee , K. Kim , W. I. Park , B. Kim , J. H. Park , T. Kim , S. Bong , C. Kim , G. Chae , M. Jun , Y. Hwang , Y. S. Jung , S. Jeon , *Nano Letters,* **2012**, 12 , 6078 .

3.9. Y. Li , Y. Zhao , H. Cheng , Y. Hu , G. Shi , L. Dai , L. Qu , *J. Am. Chem. Soc.* **2012**, 134 , 15 .

3.10. T. Gokus , R. R. Nair , A. Bonetti , M. Bohmler , A. Lombardo , K. S. Novoselov , A. K. Geim , A. C. Ferrari , A. Hartschuh , *ACS Nano* **2009**, 3 , 3963 .

3.11. D. C. Kim , D.-Y. Jeon , H.-J. Chung , Y. Woo , J. K. Shin , S. Seo , *Nanotechnology,* **2009** , 20 , 375703 .

3.12. C. Hu , Y. Liu , Y. Yang , J. Cui , Z. Huang , Y. Wang , L. Yang , H. Wang , Y. Xiao , J. Rlong , *J. Mater. Chem. B,* **2013** , 1 , 39 .

3.13. X. Yan , B. Li , X. Cui , K. Wei , L. Li , *J. Phys. Chem. Lett.,* **2011**, 2 , 1119 .

3.14. H. Tetsuka , R. Asahi , A. Ngoya , K. Okamoto , I. Tajima , R. Ohta , A. Okamoto , *Adv. Mater.* **2012**, 24 , 5333 .

3.15. S. Bae , H. Kim , Y. Lee , X. Xu , J. Park , Z. Yi , J. Balakrishnan , T. Lei , H. R. Kim , Y. I. Song , Y. Kim , K. S. Kim , B. Ozyilmaz , J. Ahn , B. H. Hong , S. Iijima, *Nature Nanotech*. **2010**, 5 , 574.

3.16. S. Horischi , T. Gotou , M. Fujiwara, *Appl. Phys. Lett.* **2004**, 84 , 2403 .

3.17. A. C. Ferrari , J. C. Meyer , V. Scardaci , C. Casiraghi , M. Lazzeri , F. Mauri , S. Piscanec , D. Jiang , K. S. Novoselov , S. Roth , A. K. Geim , *Phys. Rev.* **2006**, 97 , 187401 .

3.18. a) A. Ferrari , J. Robertson , Phys. Rev. B 2001 , 64 , 075414 ; b) C. Casiraghi , S. Pisana , K. S. Novoselov , A. K. Geim , A. C. Ferrari , *Appl. Phys. Lett.* **2007** , 91 , 233108 .

3.19. L. G. Bulusheva , A. V. Okotrub , I. A. Kinloch , A. G. Kurenya , A. G. Kudashov , X. Chen , H. Song , *Phys. Stat. Sol. b* **2008** , 245 , 1971.

3.20. U. Sim , T. Yang , J. Moon , J. An , J. Hwang , J. Seo , J. Lee , K. Y. Kim , X. Han , B. H. Hong , K. T. Nam , *Energy Environ. Sci.* **2013** , 6 , 3658 .

3.21. A. C. Nielander , M. J. Bierman , N. Petrone , N. C. Strandwitz , S. Ardo , F. Yang , J. Hone , N. S. Lewis , *J. Am. Chem. Soc.* **2013** , 135 , 17246 .

Chapter 4 Biomimetric carbon-based catalyst inspired by polydopamine

4.1. Introduction

Hydrogen fuel has been drawing significant attention within the area of sustainable energy source. In particular, hydrogen production by water splitting reaction has been researched for an eco-friendly and a sustainable energy.2 Commercialization of hydrogen production via the water splitting demands electrochemical or photoelectrochemical cell (PEC) system with high-preformance catalysts on the electrode.3 Nevertheless, previously reported carbon-based catalysts still have several drawbacks during the synthesis process. For example, carbon-based catalysts, such as graphene and graphene-based materials require multiple gas sources with precise pressure control and multiple transfer processes after their synthesis.4 Here, we suggest a carbon nanosheet (CNS) as a new hydrogen evolution catalyst for the PEC cell system based on bioinspired molecular materials. The source of the CNS can be polydopamine, which derived from adhesives protein from marine mussels. Moreover, through a variety of chemical doping processes, active sites for the hydrogen evolution reaction (HER) in the CNS can be generated, and these active sites can boost their catalytic activity with controllability.

Thermodynamically, a single-component system based on semiconductor possessing a band gap of 1.23 eV can product hydrogen and oxygen gas simultaneously through the water splitting reaction. Ti, Nb, Ta-based compounds, oxynitride, oxysulfide, and sulfide materials have been suggested as promising materials for use as photocatalysts. However, kinetically, water splitting via one single-component system is difficult to realize only using the thermodynamic potential. Alternatively, only half of the reaction, such as the oxygen evolution reaction (water oxidation reaction) or HER (proton

reduction reaction) can be investigated separately instead of attempting to analyze both evolution reactions. The other half of the reaction can be realized with the use of a sacrificial alcohol for the reduction reaction, and silver or sulfide ions for the oxidation reaction. Such inherent limitations of one-component-semiconductor approaches have opened up many possibilities for developments in the PEC cells that have photocathode and photoanode separately. This is easily implementable in terms of tenability, controllability, and efficiency. However, the kinetic problem should be considered for the operation at each half cell system. At the anodic surface, the oxidation in the water splitting reaction is

$O2 + 4e- + 4H+ \leftrightarrow 2H2O$

Eanodic = 1.23 V – 0.059 (pH value) V (vs. NHE) (1)

while the reduction reaction at the cathodic surface is

$4e- + 4H+ \leftrightarrow 2H2$ .....

Ecathodic = 0 V – 0.059 (pH value) V (vs. NHE), (2)

, where NHE is the Normal Hydrogen Electrode. The value of standard potential is varied by pH (Ehalf reaction = E – 0.059 * (pH) vs NHE). The thermodynamic potential of the water splitting reaction (Eo,cell = 1.23 V) is calculated from the difference between the equation (2) and (1). However, additional potential is kinetically required to generate a reaction at a certain rate, which is called overpotential, η. Whereas, if a current icathodic flows at the cathode, the same current of ianodic has to flow at the anode side to connect the circuit. Therefore, both the anode and cathode electrodes need the additional overpotential. The overpotentials at the both electrode are expressed as ηc and ηa, respectively. Therefore, the overall applied potential, Eapplied potential, is

Eapplied potential = 1.23 V + ηc + ηa. (3)

A higher overpotential during certain reaction should requires a higher overall applied voltage. The introduction of the catalyst for the water splitting

system can decrease the total overpotential required for the electrolysis of water.

Silicon, one of the most earth-abundant elements, can be a propitious candidate element for the development of water splitting platforms owing to its compatibility with the existing processes and its precise controllability.10 Si can be used both as a photocathode and a photoanode for photochemical water splitting with doping control and band tuning. However, the formation of native oxides on the Si surface in an aqueous solution significantly lowers its PEC performance. Moreover, the small band bending occurring at the conduction band and the redox level of the H_2/H^+ electrolyte restricts its PEC efficiency compared to the Si/non-aqueous solvent system. Consequently, the development of co-catalysts with passivation is necessary for an efficient and long-term operation.

The co-catalyst deposited on the photoelectrode can enhance the PEC performance. Pure noble metals, metal composites, alloys, nonmetallic compounds, and molecular catalysts have been used as co-catalysts for the PEC cells. To overcome economic issues, earth-abundant nonprecious metal catalysts, such as Mo3S4, Ni, and Mo have been decorated with Si pillar structures showing a high current density. However, when deposited with opaque catalysts, the limiting current density significantly decreases owing to the hindrance by the incident light and the light blocking by catalysts on the Si surface.

To address the limitations of the previous catalysts, non-metal carbon-based catalysts have been tested as environmentally benign, non-precious, and durable catalysts. Among carbon-based catalysts, a reduced graphene oxide containing catalytically active materials or sites exhibited improved activity in HERs, oxygen evolution reactions, and oxygen reduction reactions. However, in most cases, the previously used carbon materials showed limited success as electrically conductive substrates or supporters that increase the

performance of other decorated active catalytic materials. Recently, we developed new graphene quantum sheets as an electrocatalyst for efficient HER, and investigated the effects of hetero atom (nitrogen) doping, disorders and defects generated via N_2 plasma, which improved the catalytic activity. Nevertheless, the challenge associated with the previous carbon-based catalysts, such as graphene and graphene- based materials lies in the complicated and inefficient synthesis requiring multiple transfer processes and low throughput. Chemical Vapor Deposition (CVD)-grown pristine graphene as a starting material requires very stringent fabrication conditions and high cost. To produce more efficient catalysts for HER, we should investigate candidates that can be easily synthesized with inexpensive starting materials. Here, inspired by the biomolecular system, we suggest a biomimetic 2D carbon nanosheet as a new hydrogen evolution catalyst layer for the PEC cell system. The CNS is synthesized using polydopamine. Moreover, active sites for the HER in the CNS enhance its catalytic activity with controllability.

4.2 Results and Discussion

Synthesis of carbon nanosheet from polydopamine was referred to the literature method and modified detail process to make active sites for hydrogen evolution reaction. SiO_2/Si target substrate was immersed in tris-(hydroxy-methyl) aminomethane solution (10 mM, pH 8.5) mixed with dopamine (2 mg). Then, polydopamine films were deposited on the surface of the target substrate. The thickness of the film could be controlled as a function of the immersion time. For carbonization, sample were then placed in a tube furnace for thermal treatment at elevated temperatures in a nitrogen atmosphere.

The observation of natural phenomena can be breakthrough for discovery of novel materials and pathway of innovative technology. Among the many

biomimetic researches, surface coating process using by polydopamine which motivated by mussel adhesives proteins (MAPs) is suitable examples of this discovery.[8.23] Mussel can adhere to virtually all types of surfaces by secreting adhesives protein. Figure 4.1 (a) shows mussel attached to rock surface by secreting adhesive proteins (MAPs). MAPs are composed to several amino acids, which are abundant in 3,4-dihydroxy-L-phenylalanine (DOPA) and lysine as shown in Figure 4.1 (b). By oxidative polymerization leading to bulk solidification, DOPA and other catechol compound can covalently (or noncovalently) attached to diverse surface. Polydopamine has similar structure with naturally occurring melanin (eumelanin) that incorporates many functional groups such as catechol, hydroxyl, amine and imine (Figure 4.1 (c)). Polydopamine film was obtained according to below procedure as shown in Figure 4.1 (d). First, Dopamine as monomer is added into an alkaline solution and oxidized with oxygen as oxidant without any complicated reactant or harsh condition. Oxidized dopamine immediately turns into quinone form which can be oligomer, and finally coated on substrate with dense polymer film. This hetero-aromatic polymer film can be controllably coated on several substrates in the thickness range of a few tens of nanometer depending on the immersion time. For the preparation of the N-doped carbon nanosheet, polydopamine coated substrate is pyrolyzed in tube furnace under H_2 and Ar atmosphere.

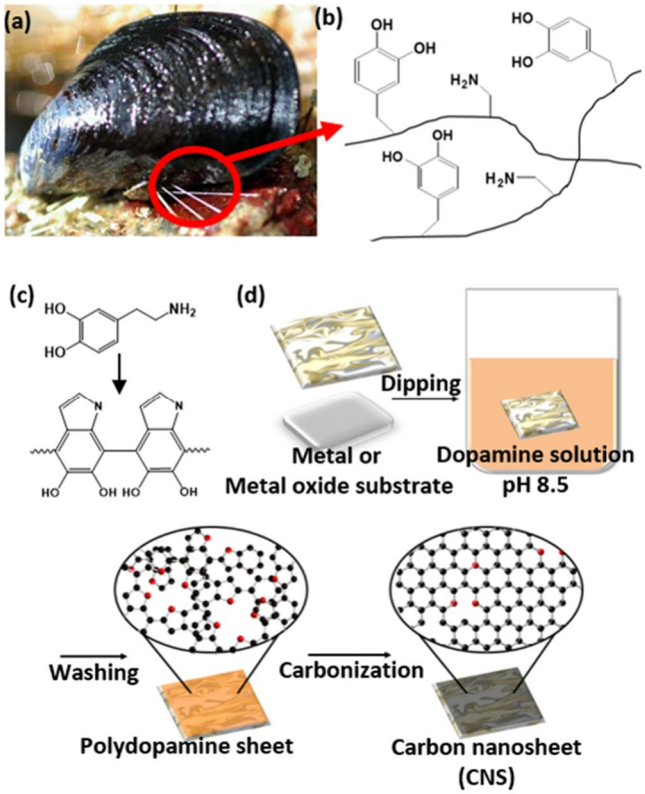

Figure 4. 1. Schematic of a structure of polydopmaine and a synthetic process of carbon nanosheets. (a) Photograph of a marine mussel secreting adhesives protein. (b) Structural proposal of mussel adhesives protein (MAPs). (c) Schematic illustration of polydopamine as MAPs analogues by polymerization. (d) Schematic illustration of the synthetic process for carbon nanosheet from polydopamine

After carbonization of polydopamine film, the D peak (disordered carbon) was significantly increased in Raman spectra, the generation of defects and edges by the H_2/Ar treatment during annealing is also identified (Figure 4.2 (a)). The intensity ratio of D peak (1380 cm^{-1})/G peak (1600 cm^{-1}) (I_D/I_G ratio) indicates the extent of the carbonization, which is the extent of crystallization of sp2 phase.[8.22] Carbon nanosheet shows 0.97 of I_D/I_G ratio with both sharp peaks, while pristine polydopamine sample shows 0.69 of I_D/I_G ratio. This D-to-G Peak intensity ratio (I_D/I_G) of carbon nanosheet indicated that polydopamine film successfully transforms into graphitic structure, which is similar with chemical structure of graphene.[8.24] Chemical structural analysis of polydopamine and carbon nanosheet is performed by measurement of X-ray photoelectron spectroscopy (Figure 4.2 (a)-(f)). The peak of C 1s, N 1s and O 1s, obtained on the polydopamine film were shown in Figure 4.2 (c) and 8.2 (e). Primary N (401.7 eV), secondary N (399.6 eV) and tertiary/aromatic N (398.2 eV) in N S1 spectrum of polydopamine indicate that nitrogen-to carbon ratio is ~11%. N S1 originated from polydopamine is dominated with secondary amine at 399.6 eV, and include low amount of tertiary or aromatic amine. Also, a large amount of hydroxyl functional group can be measure in C 1s. These functional groups such as hydroxyl, primary amine, and other dangling bonds have low stability in annealing condition. These unstable functional groups are converted to more stable conformation (secondary N or tertiary/aromatic N) or detached from polymer matrix. In case of carbon nanosheet, low oxygen contents and high aromatic amine were measured at N 1s and C 1s, it means that polydopamine is reduced and transformed into graphitic structure during heat treatment. As a result of thermal reduction, nitrogen-to-carbon ratio is ~6% in N_1 spectrum of carbon nanosheet.

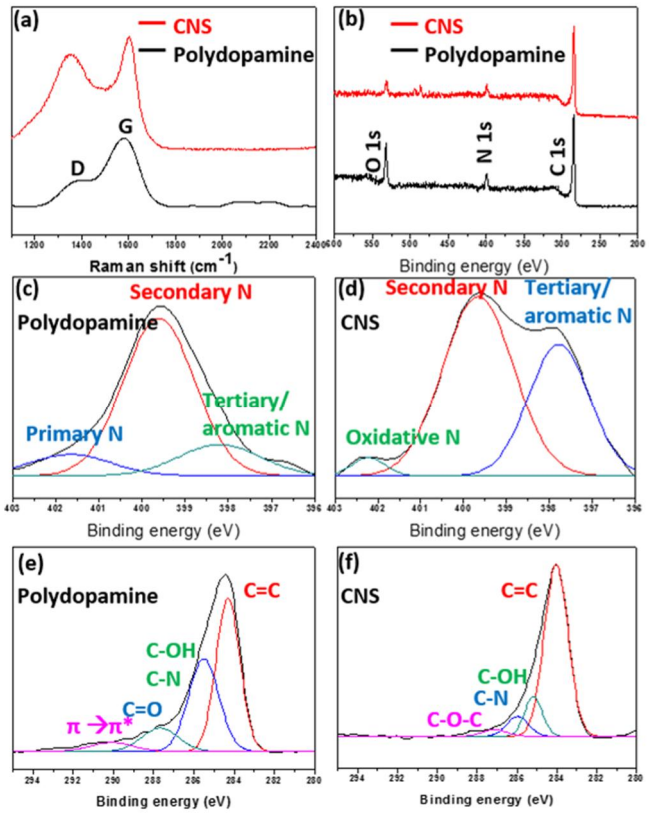

Figure 4. 2. Surface characterization of the polydopamine and the carbon nanosheets (a) Raman spectra and (b) XPS spectra of polydopamine and carbon nanosheet. (c)-(d) High-resolution N1 peak of polydopamine and carbon nanosheet

To investigate surface analysis, AFM measurement is conducted. AFM images of polydopamine film shows 28 nm thickness and low RMS of nm on SiO_2/Si substrate, which is substantially uniform coating behavior (Figure 4.3 (a)). After carbonization, AFM images for the surface of carbon nanosheet show that the thickness of carbon nanosheet is approximately 10 nm with a relative smooth surface (Figure 4.3 (b)). Plenty of carbon aggregations are also shown on the sheet during annealing process (white islands in the image).

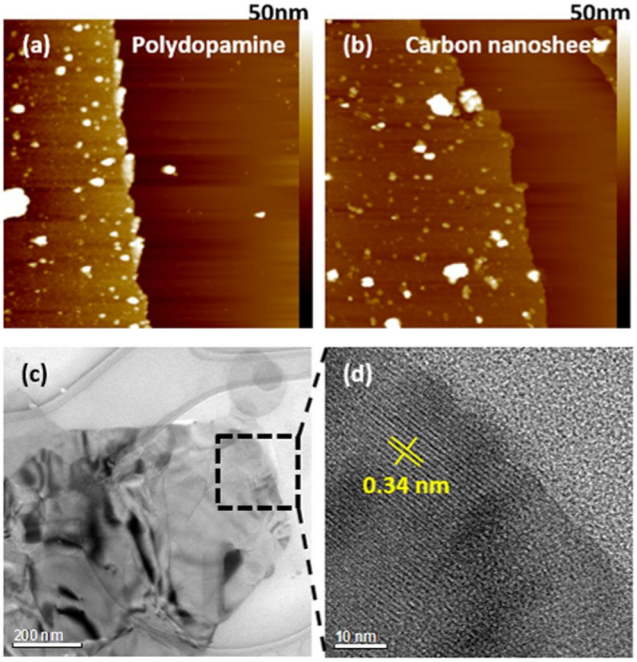

Figure 4. 3. AFM images of (a) polydopamine, (b) carbon nanosheet. (c) and (d) TEM image of carbon nanosheet from pyrolysis of polydopamine.

For further characterization of atomic structure, TEM is measured (Figure 4.3 (c) and (d)). The sample was prepared by conventional CVD graphene transfer method on TEM grid. Figure 4.3 (a) shows TEM images of carbonized polydopamine nanosheet which was annealed at 800 ℃ for 1h in

a heating rate of 10 ℃. The magnified image shows that carbonized film had clear atomic lattice structure and its layer distance was approximately 0.34 nm, which is distance between graphite stacking layers (Figure 4.3 (d)).[8.25]

To evaluate the photocathodic behavior of carbon nanosheet loaded on a p-type Si electrode (CNS-Si), a current density was measured as the potential was swept from 0.4 V to -1.0 V vs. Reversible Hydrogen Electrode (RHE) using cyclic voltammetry. As shown in Figure 4.1 (a), the current density of the bare Si increases gradually from -0.2 V vs. RHE and is saturated at approximately -35 mA/cm^2 below -1.0 V, vs. RHE, as a potential is negatively applied. Interestingly, in the measurement of CNS-Si, the overall current density-potential (*J-E*) curve is shifted by approximately 0.2 V toward the positive potential. The onset potential (V_{os}) is defined as the potential at the photocurrent density of -1 mA/cm^2. As shown in Figure 4.4 (a), V_{os} is 0.21 V vs. RHE, and this V_{os} is a positive shift by 0.38 V compared to that of bare Si (-0.17 V vs. RHE). To our knowledge, the value of 0.29 V is the best among the extent of shifts by carbon-based catalysts. This result showed solar-to-hydrogen conversion efficiency of 0.59 %. Although reduced graphene oxide and carbon nanotube have been applied to silicon photoelectrodes as catalysts, the performances of these catalysts are not comparable to those of precious metal catalysts.[8.26] Additionally, for previously reported carbon-based catalysts, the insufficient activity remain unsolved. Our result showing the increase of V_{os} indicates that carbon nanosheet acts as an effective catalyst for HERs on the Si photocathode.

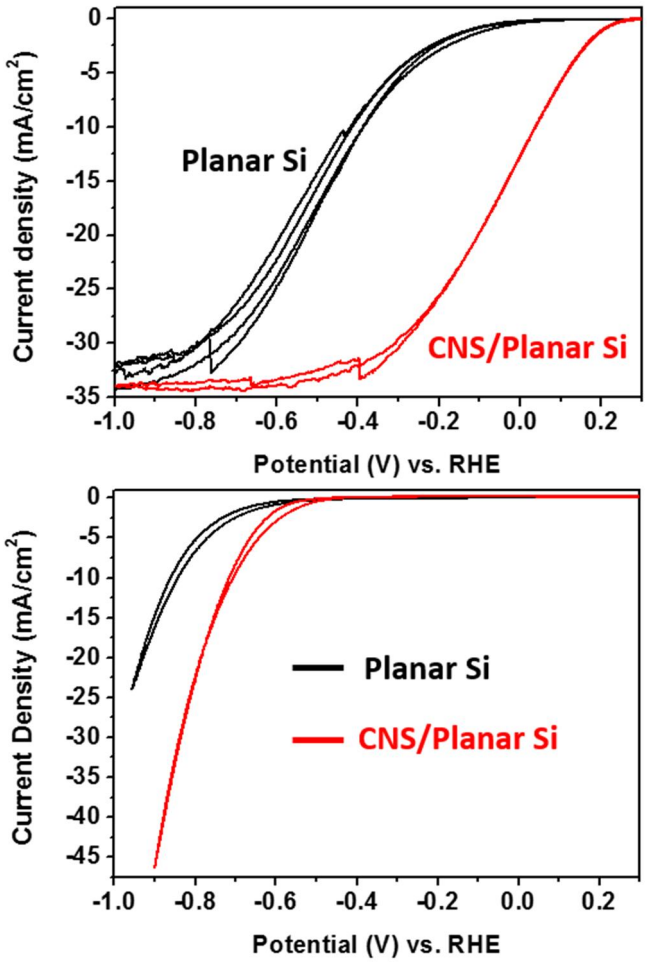

Figure 4. 4. Cyclic Voltammetry (CV) of bare Si and carbon nanosheet (CNS) on a Si electrode. (a) Photocurrent density-potential (*J-E*) curves for the lightly boron doped p-Si electrode deposited with CNS and without any catalysts, respectively. (b) Polarization curves of bare and CNS on heavily arsenic doped n^+ type Si electrodes under dark condition. Each CV was performed at a scan rate of 0.05 V/sec.

To investigate the electrocatalytic activity of CNS, we measured cyclic voltammetry (CV) without illumination with a rotating disk electrode system (RDE). To fabricate the working electrode, CNS was transferred to a glassy carbon tip that is inert in aqueous solution. An additional positive shift in the onset potential by CNS is also observed in the RDE measurements. As shown in Figure 4.5 (a), the potential to attain current density of -5 mA/cm^2 is -0.25 V vs. RHE; this value is 80 mV larger than that of the bare glassy carbon (-0.33 V vs. RHE). For comparison, representative carbon-based catalyst, RDE of pristine graphene was also measured and carbon nanosheet shows 30 mV larger than that of the graphene material (-0.28 V vs. RHE, not shown here), which shows the catalytic activity of CNS is slightly better than that of monolayer graphene. [8.6]

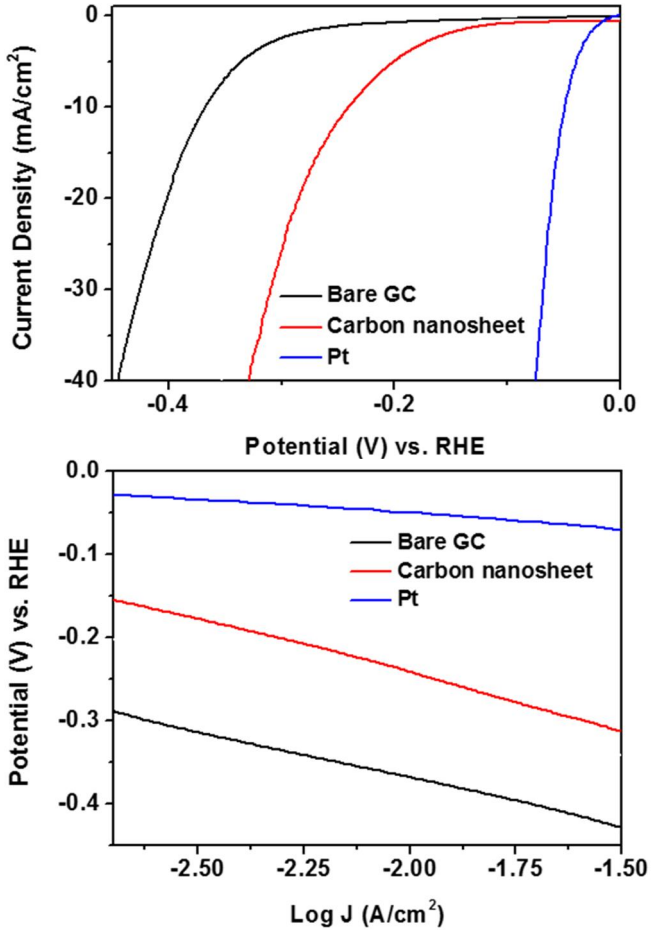

Figure 4. 5. Electrochemical activity of carbon nanosheet (CNS) on Glassy Carbon (GC) electrode from rotating disk electrode system. (a) CV curve of bare, CNS, and Pt/C on GC. (b) Tafel plots were derived from (a) CV data.

The *J-E* curves in Figure 4.5 (a) is converted into a plot of the potential as a function of the logarithm of *J*, to quantitatively gain more insight into the catalytic activity of CNS. This plot is called a Tafel plot. The measured potentials are corrected for the ohmic potential drop losses that originated from the resistance of the interface between the substrate and the electrolyte. Analysing the impedance spectroscopy reveals that the resistances of the bare glassy carbon (GC) and CNS on GC are 13.0 and 13.2 ohm, respectively. The Tafel plot provides two parameters to estimate the electrocatalytic activity: the Tafel slope and the exchange current density. The Tafel slope is defined to be a measure of the potential increase required to increase the resulting current by 1 order of magnitude. [8.27] The bare GC shows a Tafel slope of 85 mV/decade, and CNS-GC exhibited a 7 mV/decade lower Tafel slope (78 mV/decade) than that of bare GC. For the comparison with the well-known catalyst, Pt particles were deposited on GC and the electro-catalytic activity was analysed. The applied potential to obtain -5 mA/cm^2 is -0.04 V vs. RHE, which is shifted positively by 0.24 V compared to that of CNS-GC. The Tafel slope of Pt-GC is 42 mV/decade, which is a 32 mV/decade lower than that of CNS-GC. The Tafel slope is an inherent property of the catalyst that is determined by the rate-limiting step for HER. Mechanistically, for the HER in acidic solution, the following possible reaction steps have been suggested: [8.28]

$$H_3O^+ + e^- \rightarrow H_{ads} + H_2O \qquad (4.1)$$

$$H_{ads} + H_3O^+ + e^- \rightarrow H_2 + H_2O \qquad (4.2)$$

$$H_{ads} + H_{ads} \rightarrow H_2 \qquad (4.3)$$

where H_{ads} is the adsorbed hydrogen atom. (4.1) is a discharge step (the Volmer reaction), (4.2) is a desorption step (the Heyrovsky reaction), and (4.3) is a recombination step (the Tafel reaction). The value of the Tafel slope also relates to the adsorbed hydrogen coverage (θ_H) on the surface of electrode. If the recombination of adsorbed hydrogen (the Tafel reaction) is the rate-determining step for the HER and if the coverage is very high ($\theta_H \approx 1$), the

measured Tafel slope is 30 mV/decade. However, if the electrochemical desorption step (the Heyrovsky reaction) is the rate-determining step, a Tafel slope of 118 ~ 40 mV/decade is measured and is dependent of the value of θ_H (0 ~ 1).[8.17] The observed Tafel slope of ~80 mV/decade in the current work indicates that the kinetics of the HER on bare GC and CNS-GC electrodes is determined by the Heyrovsky reaction because θ_H has an intermediate value. Specifically, HER using catalyst (Cat.) can be described as follows:[8.29]

$Cat. + H^+ + e^- \rightarrow H\text{-}Cat.$, Volmer reaction (4.4)

$2(H\text{-}Cat.) \rightarrow H_2 + 2Cat.$, Tafel reaction (4.5)

$H\text{-}Cat. + H^+ + e^- \rightarrow H_2 + Cat.$, Heyrovsky reaction (4.6)

In the Volmer-Heyrovsky mechanism, the proton from the electrolyte solution is discharged on the catalyst surface to form an adsorbed hydrogen atom. This step is followed by combination with another proton and electron to form molecular hydrogen.

The improvement in the catalytic activity with CNS is also confirmed by the comparison of exchange current density in the Tafel plot. HER activity of the catalyst can be characterized by representative parameters; the exchange current density and the bond energy of hydrogen adsorbed to the catalyst. During hydrogen evolution, a current I can be described as:[8.30]

$$I = -e(r+ - r-) \quad (4.7)$$

where, r+ - r- is the net rate of Eq. (4.7). The exchange current is the forward and backward rate when Eq. (4.7) is in equilibrium. The ability of a given metal to catalyze the hydrogen evolution reaction is usually measured by the exchange current density, which is the rate of hydrogen evolution per surface area at the electrode potential when the reaction is at equilibrium. The exchange current density (J_0) is defined to be the current density at zero overpotential. The catalytic effect originates from improving the rate of charge transfer at the interface between the electrode and electrolyte or from lowering the activation energy barrier for a chemical reaction; these catalytic

effects are represented by J_0. The higher J_0 indicates that electron transfer or the adsorption/desorption of protons at the electrode/electrolyte can occur more easily with a lower kinetic barrier. From the Tafel plot, J_0 can be obtained by extrapolating the plot in Figure 4b and extracting the current density at 0 V vs. RHE. The CNS-GC electrode shows an enhanced J_0 of 2.9×10^{-6} A/cm^2, which is higher than the J_0 of bare GC (1.63×10^{-6} A/cm^2). The J_0 of CNS is also compared with that of the monolayer graphene. J_0 of monolayer graphene is similar to exchange current density of CNS (2.7×10^{-6} A/cm^2). We are currently investigating to identify and quantify the active sites of CNS. From the Tafel analysis, CNS has the catalytic activity for the HER compared to that of the previous graphene based catalyst.

The passivation effect of CNS was also investigated. A chronoamperometray test of the bare Si and CNS-Si was also performed at 0 V vs. RHE (Figure 4.6 (a)) and the current densities normalized by their initial values were displayed as a function of time in Figure 4.6 (b). CNS-Si shows the suppressed degradation of the performance in the photocurrent density compared to that of the bare Si at pH 0 condition. The performance of the bare Si completely fails only after 1,000 sec. The CNS-Si electrode maintains more than 20% of the normalized current and -4 mA/cm^2 even at 6,000 sec. Thus, from the change of the current density at 0 V vs. RHE, it is known that CNS suppresses the degradation of the photoelectrochemical performance by the oxidation of Si surface.

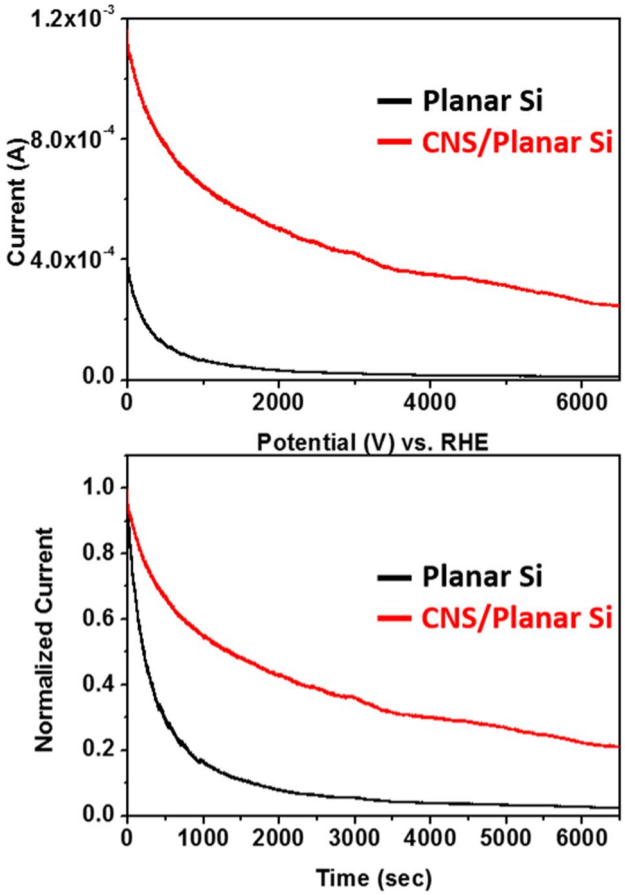

Figure 4. 6. Chronoamperometry test of bare planar Si and CNS on Si photocathodes. (a) The change of photocurrent density at 0 V vs. RHE of bare planar Si (black line) and CNS-Si (red line) electrodes with the increase of time at 0. (b) The change of normalized photocurrent density (*J* divided by initial *J*) at 0 V vs. RHE with the increase of time at pH 0. The initial *J* is the initial current density in the chronoamperometry test.

To confirm the passivation effect of CNS on Si surface, the surface state of Si was investigated before and after the chronoamperometry test at 0 V vs. RHE for 6,000 sec. XPS spectra of bare Si and CNS-Si were measured in the Si $2p_{3/2}$ region. The Si peak can be assigned at 99.3 eV, and SiO_2 peak can be assigned at 103.3 eV. From XPS spectra of bare Si, the peak of Si-O increases after the chronoamperometry test. In case of CNS-Si samples, after the long-term test, there is only slight increase in the Si-O peak. These results indicate that graphene suppresses the oxidation of Si surface during the photoelectrolysis.

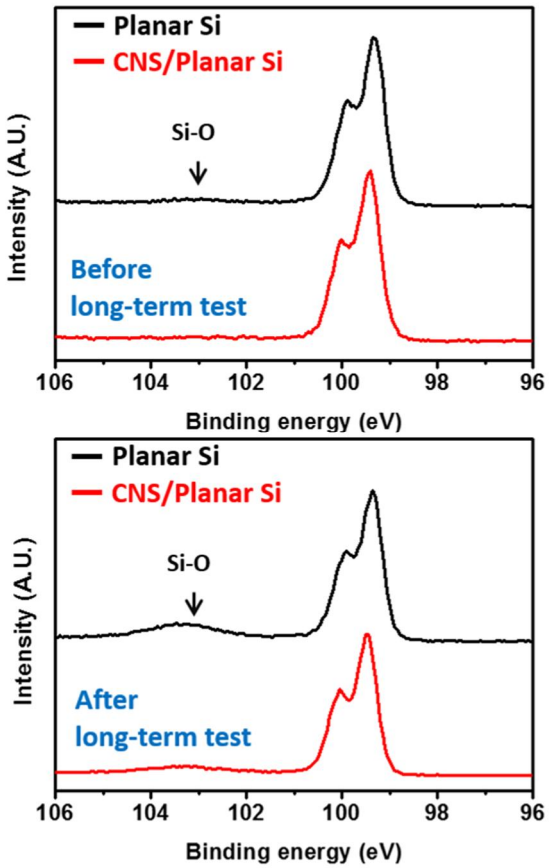

Figure 4. 7. High resolution XPS spectra of Si 2p region of bare planar Si and CNS-Si electrodes. XPS spectra of each sample (a) before the chronoamperometry test and (b) after the chronoamperometry test at 0 V vs. RHE for 6,000 sec. Narrow-scan data of the Si 2p region were collected using pass energy of 40 eV and 0.05 eV/step.

4.3 Conclusion

We have presented carbon nanosheets as a catalyst for solar-driven hydrogen evolution reaction on Si photocathode. Carbon nanosheet has an excellent catalytic activity for photoelectrochemical cell. Our approach in this study exploits a strategy to develop metal-free carbon-based catalysts with high efficiency for solar-driven hydrogen fuel production.

Bibliography

4.1. Heller, A. Aharon-Shalom, E. Bonner, W. A. and Miller, B., Hydrogen-evolving semiconductor photocathodes: nature of the junction and function of the platinum group metal catalyst. *J. Am. Chem. Soc.* **104**, 6942-6948 (1982)

4.2. Hou, Y. Abrams, B. L. Vesborg, P. C. K. Björketun, M. E. Herbst, K. Bech, L. Setti, A. M. Damsgaard, C. D. Pedersen, T. Hansen, O. Rossmeisl, J. Dahl, S. Nørskov, J. K. and Chorkendorff, I., Bioinspired molecular co-catalysts bonded to a silicon photocathode for solar hydrogen evolution. *Nature Mater.* **10**, 434-438 (2011)

4.3. Reece, S. Y. Hamel, J. A. Sung, K. Jarvi, T. D. Esswein, A. J. Pijpers, J. J. H. and Nocera, D. G., Wireless Solar Water Splitting Using Silicon-Based Semiconductors and Earth-Abundant Catalysts. *Science* **334**, 645-648 (2011)

4.4. Li, Y. Wang, H. Xie, L. Liang, Y. Hong, G. and Dai, H., MoS2 nanoparticles grown on graphene: an advanced catalyst for the hydrogen evolution reaction. *J. Am. Chem. Soc*. **133**, 7296-7299 (2011)

4.5. Li, R. Parvez, K. Hinkel, F. Feng, X. and Mullen, K. Bioinspired wafer-scale production of highly stretchable carbon films for transparent conductive electrodes. *Angew. Chem. Int. Ed*. **52**, 5535–5538 (2013)

4.6. Sim, U.; Yang, T.-Y.; Moon, J.; An, J.; Hwang, J.; Seo, J.-H.; Lee, J.; Kim, K. Y.; Lee, J.; Han, S.; Hong, B. H.; Nam, K. T., N-doped monolayer graphene catalyst on silicon photocathode for hydrogen production. *Energy & Environmental Science* 2013, **6** (12), 3658-3664.

4.7. Fujishima, A.; Honda, K., Electrochemical photolysis of water at a

semiconductor electrode. *Nature* **238**, 37-38, (1972)

4.8. Maeda, K.; Domen, K., Photocatalytic water splitting: recent progress and future challenges. *J. Phys. Chem. Lett.* **1**, 2655-2661, (2010)

4.9. Kudo, A.; Miseki, Y., Heterogeneous photocatalyst materials for water splitting. *Chem. Soc. Rev.* **38**, 253-278, (2009)

4.10. Allam, N. K.; Poncheri, A. J.; El-Sayed, M. A., Vertically oriented Ti–Pd mixed oxynitride nanotube arrays for enhanced photoelectrochemical water Splitting. *ACS Nano* **5**, 5056-5066, (2011)

4.11. Yun, H. J.; Lee, H.; Kim, N. D.; Lee, D. M.; Yu, S.; Yi, J., A combination of two visible-light responsive photocatalysts for achieving the Z-Scheme in the solid state. *ACS Nano* **5**, 4084-4090, (2011)

4.12. Walter, M. G.; Warren, E. L.; McKone, J. R.; Boettcher, S. W.; Mi, Q.; Santori, E. A.; Lewis, N. S., Solar water splitting cells. *Chem. Rev.* **110**, 6446-6473, (2010)

4.13. Hou, Y.; Abrams, B. L.; Vesborg, P. C. K.; Björketun, M. E.; Herbst, K.; Bech, L.; Setti, A. M.; Damsgaard, C. D.; Pedersen, T.; Hansen, O.; Rossmeisl, J.; Dahl, S.; Nørskov, J. K.; Chorkendorff, I., Bioinspired molecular co-catalysts bonded to a silicon photocathode for solar hydrogen evolution. *Nat. Mater.* **10**, 434-438, (2011)

4.14. Chen, Y. W.; Prange, J. D.; Dühnen, S.; Park, Y.; Gunji, M.; Chidsey, C. E. D.; McIntyre, P. C., Atomic layer-deposited tunnel oxide stabilizes silicon photoanodes for water oxidation. *Nat. Mater.* **10**, 539-544, (2011)

4.15. Matsumura, M.; Roy Morrison, S., Anodic properties of n-Si and n-Ge electrodes in HF solution under illumination and in the dark. *J. Electroanal. Chem. and Inter. Electrochem.* **147**, 157-166, (1983)

4.16. Boettcher, S. W.; Warren, E. L.; Putnam, M. C.; Santori, E. A.; Turner-Evans, D.; Kelzenberg, M. D.; Walter, M. G.; McKone, J. R.; Brunschwig, B. S.; Atwater, H. A.; Lewis, N. S., Photoelectrochemical hydrogen evolution using Si microwire arrays. *J. Am. Chem. Soc*. **133**, 1216-1219, (2011)

4.17. Cook, T. R.; Dogutan, D. K.; Reece, S. Y.; Surendranath, Y.; Teets, T. S.; Nocera, D. G., Solar energy supply and storage for the legacy and nonlegacy worlds. *Chem. Rev*. **110**, 6474-6502, (2010)

4.18. Novoselov, K. S.; Geim, A. K.; Morozov, S. V.; Jiang, D.; Katsnelson, M. I.; Grigorieva, I. V.; Dubonos, S. V.; Firsov, A. A., Two-dimensional gas of massless Dirac fermions in graphene. *Nature* **438**, 197-200, (2005)

4.19. Liang, Y.; Li, Y.; Wang, H.; Zhou, J.; Wang, J.; Regier, T.; Dai, H., Co_3O_4 nanocrystals on graphene as a synergistic catalyst for oxygen reduction reaction. *Nat. Mater*. **10**, 780-786, (2011)

4.20. Qiu, J.-D.; Wang, G.-C.; Liang, R.-P.; Xia, X.-H.; Yu, H.-W., Controllable Deposition of platinum nanoparticles on graphene as an electrocatalyst for direct methanol fuel cells. *J. Phys. Chem. C* **115**, 15639-15645, (2011)

4.21. Xiang, Q.; Yu, J.; Jaroniec, M., Graphene-based semiconductor photocatalysts. *Chem. Soc. Rev*. **41**, 782-796, (2012)

4.22. Li, R.; Parvez, K.; Hinkel, F.; Feng, X.; Müllen, K., Bioinspired wafer-scale production of highly stretchable carbon films for transparent conductive electrodes. *Angew. Chem. Int. Ed*. **52**, 5535-5538, (2013)

4.23. Lee, H.; Dellatore, S. M.; Miller, W. M.; Messersmith, P. B., Mussel-inspired surface chemistry for multifunctional coatings. *Science*, **318**, 426-430, (2007)

4.24. Yu, X.; Fan, H.; Liu, Y.; Shi, Z.; Jin, Z., Characterization of

carbonized polydopamine nanoparticles suggests ordered supramolecular structure of polydopamine. *Langmuir* **30**, 5497-5505, (2014)

4.25. Huang, J. Y., HRTEM and EELS studies of defects structure and amorphous-like graphite induced by ball-milling. *Acta Materialia* **47**, 1801-1808, (1999)

4.26. Huang, Z.; Zhong, P.; Wang, C.; Zhang, X.; Zhang, C., Silicon nanowires/reduced graphene oxide composites for enhanced photoelectrochemical properties. *ACS Appl. Mater. & Inter*. **5**, 1961-1966, (2013)

4.27. Allen J. Bard, L. R. F., *Electrochemical methods: fundamentals and applications*. John Wiley & Sons, Inc. **864**, (2001)

4.28. Li, Y.; Wang, H.; Xie, L.; Liang, Y.; Hong, G.; Dai, H., MoS2 nanoparticles grown on graphene: an advanced catalyst for the hydrogen evolution reaction. *J. Am. Chem. Soc*. **133**, 7296-7299, (2011)

4.29. J. Larminie, A. Dicks, M. S. McDonald, *Fuel cell systems explained*, Vol. **2**, Wiley New York, 2003.

4.30. Nørskov, J. K.; Bligaard, T.; Logadottir, A.; Kitchin, J. R.; Chen, J. G.; Pandelov, S.; Stimming, U., Trends in the exchange current for hydrogen evolution. *J. Electrochem. Soc*. **152**, J23-J26, (2005)

Chapter 5 Cu(II)-complexed Polydopamine for HER catalysts

5.1. Introduction

Hydrogen energy has been drawing much attention in renewable energy t echnologies. Especially, hydrogen production by water splitting reaction ha s been widely studied as environmental and sustainable energy source.[5.1] T o increase catalytic activity for hydrogen production, current studies are fo cused on developing the efficient the earth-abundant based-catalyst for alte rnating Pt based catalyst, which facilitate HER effectively in a wide pH ra nge.[5.2-5.4] Especially, the neutral water condition is highly abundant and en vironmentally friendly, which makes it suitable for hydrogen production. Nature hydrogenase enzymes possess HER properties in neutral pH conditi on with highly efficient catalytic activity. Inspired by naturally hydrogen g eneration on hydrogenase enzymes, great efforts have been devoted to fin d highly efficient catalyst based on bioinspired metal complex HER cataly st, including cobaltoxime[5.5] cobalt diamine-dioxime and nickel phosphine c ompounds[1.6], which have specific HER active site such as Co-N4, Ni-P4[5.7]. Very recently, few Cu-based HER catalyst have been reported and they h ad shown efficient activity and stability.[5.8-5.9] The observation of natural p henomena can be breakthrough for discovery of novel materials and path way of innovative renewable energy technology. Among the many biomim etic researches, surface coating process using polydopamine (PDA) which motivated by mussel adhesive protein (MAPs) is suitable examples for thi s discovery.[5.10] Polydopamine (PDA), which is an eco-friendly, biomimetic mussel adhesive molecule, can be easily synthesized by oxidative polyme rization of dopamine under alkaline aqueous condition. By oxidative poly merization of dopamine, DOPA and other catechol compound can covalen

tly (or noncovalently) attached to diverse surface. PDA is also found in m ain pigment of naturally occurring melanin (eumelanin) and has hetero-aro matic structure with many functional groups such as catechol, o-quinone, amino, and imine group.[5.11] These structural features are related with its p hysicochemical properties. In recent researches, PDA derivatives, which ha ve similar chemical structure with mussel adhesive protein, also have been considered as surface-independent coating materials. Mussels can strongly attach to diverse substrates with high binding strength in aqueous conditi on. These unique binding mechanism is related with specific adhesive prot ein which contain 3,4-dihydroxy-L-phenylalanine (DOPA) and lysine.[5.12-5.13] Many functional groups in PDA including catechol, quinone, amine, and imine serve binding site for various multivalent metal ion such as Mn^{2+}, Cu^{2+}, Fe^{3+} and Ti^{4+} etc. Moreover, many research was conducted on the m echanical role of metal ions in PDA analogues.[1.14]

Here, inspired by biomolecular system based on mussel adhesive protein, we prepared transition metal-complexed PDA matrix (M-PDA) as a new hydrogen evolution catalyst and investigated HER catalytic properties in n eutral pH condition. Through oxidative polymerization of dopamine, we sy nthesized PDA with various transition metal such as Co^{2+}, Cu^{2+}, Mn^{2+}, Ni^{2+}, and Fe^{3+} ion. Moreover, Cu(II)-PDA complex show the lowest overpote ntial for HER among these M-PDAs. To the best of our knowledge, there is no previous studies on the application of biomimetic PDA derivatives t o hydrogen production catalysts, and the overpotential of Cu(II)-PDA is lo west value among copper-based electrocatalysts for hydrogen production. This significant enhancement achieved in this study emphasizes the new p ossibilities for the application of bioinspired materials as hydrogen evoluti on reaction catalyst as well as molecular precursor approach.

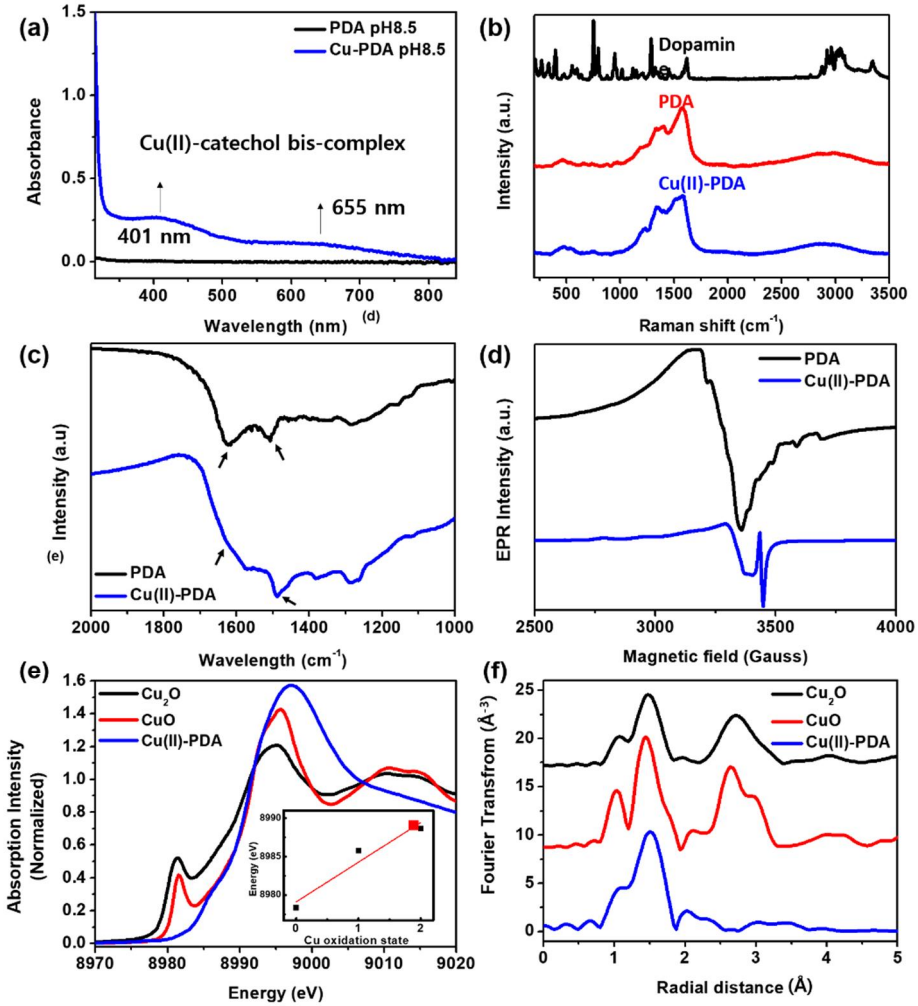

Figure 5. 1. (a) Uv-vis spectra of PDA and Cu(II)-PDA at pH 8.5 in tris buffer solution (b) Raman spectra of dopamine, PDA, and Cu(II)-PDA, (c) FT-IR spectra of PDA and Cu(II)-PDA (d) EPR spectra of PDA and Cu(II)-PDA, (e) XANES of Cu_2O, CuO, and Cu(II)-PDA, (f) EXAFS spectra of Cu_2O, CuO, and Cu(II)-PDA

5.2 Results and Discussion

Polydopamine (PDA) and Cu(II)-PDA were synthesized through the oxidative polymerization of dopamine (DA) at pH 8.5 tris buffer solution in the present of Cu^{2+} chloride. Under oxidative polymerization of DA, PDA can covalently attach to electrode surface. PDA has similar structure with naturally occurring melanin (neuromelanin) that incorporates many types of structural units such as uncycled amine containing group, cyclized indole group. (Figure 5.5) In the preparation of Cu-PDA, with $CuCl_2$, the solution initially showed pale blue, which forms the mono complex. Upon addition of tris, the solution turned a brownish yellow. Finally, the Cu(II)-PDA structure was synthesized by further titration with NaOH to pH 8, which the solution turned to greenish-yellow. The UV-vis absorbance spectrum of this solution shows an absorption band at ~402 and 635 nm that was consistent with formation of bis-complex Cu(II)-catechol predominately.[5.15] (figure 5.1 a) The formation of PDA structure was investigated by Raman spectroscopy. As shown in Figure 5.1 (b), PDA and Cu(II)-PDA show intense broad band at 1580 cm^{-1} result from stretching mode of aromatic PDA ring and disordered-induced peak at 1373 cm^{-1}. Chemical composition of Cu(II)-PDA was performed by measurement of X-ray photoelectron spectroscopy (Figure 5.1). Cu content in Cu(II)-PDA, as quantitatively determined by XPS analysis, is 1.70 at%. High resolution XPS of Cu 2p3 peak was shown in Fig Si 1b. The peak of Cu 2p3/2 and 2p1/2 could be deconvoluted with two parts, 934.8, 954.5 eV for Cu^{2+} and 932.9, 952.4 eV for Cu^{1+} or Cu^{0}.[9] These results indicated that the most of Cu^{2+} ion is complexed in PDA matrix and only small part of Cu^{1+} or Cu^{0} is formed due to reduction of Cu^{2+} during oxidative polymerization of DA. The peak of C 1s, N 1s and O 1s, obtained from PDA was shown in Fig Si 1a. N 1s originated from PDA is dominated with secondary amine at 399.6 eV and include low amount of tertiary of aromatic amine. O1s band of PDA is around 400 eV, whereas for the Cu(II)-PDA

complex, O 1s and N 1s band shifts to about 531.5 eV and 399.6 eV respectively, representing that the Cu^{2+} ion is complexed into both O and N species of PDA matrix. The chemical functional groups of PDA and Cu(II)-PDA were confirmed by FT-IR. (Figure 5. 1c) As for PDA sample, the absorption peak at 1508 and 1620 cm^{-2} are related to the stretching vibration of the indoline and indole structure in PDA. As for Cu(II)-PDA, the size of band at 1620 cm^{-2} was reduced and a new band at 1488 cm^{-2} was formed. These band intensity change and new band formation in FT-IR spectra imply the formation of the Cu(II)-PDA complex and can be found in the previously reported literature.[5.16] PDA, a type of melanin, is known to possess stable free radical structure from the comproportionation equilibrium.[5.17] The unpaired electron localized on catechol group in PDA structural unit is the paramagnetic center. To investigate the chemical interaction between the PDA and paramagnetic metal ions, the EPR spectrum of PDA and Cu(II)-PDA is measured. As shown in Figure 5. 1d, a single broad peak of PDA sample was detected. According to previous literature, the amplitude of EPR signal of PDA can decrease by adding paramagnetic ion. In case of Cu(II)-PDA, the decline of paramagnetic centers in PDA was measured with incorporating of paramagnetic Cu^{2+} ion, indicating that this quenching of EPR intensity could correspond to form Cu(II)-PDA complex.[5.18] Therefore, these results can be attributed that the Cu ion is participated in metal-PDA bonding. X-ray absorption near-edge structure (XANES) and Extended x-ray absorption fine structure (EXAFS) spectra at Cu Kα edge were measured to understand the local structure of Cu complex in PDA matrix compared with Copper oxide. Figure 5. 1e shows the XANES spectra of Cu(II)-PDA and other two Cu oxide standard samples. Compared to the oxidation number of Cu oxide standard sample, the oxidation number of Cu ion in PDA matrix was found to be 1.81. It is found that almost Cu atom is chelated as Cu^{2+} ion in PDA matrix and partially reduced to Cu^{0} and/or Cu oxide as similar results in previous

literature.[5.19] Figure 5.1 f shows the EXAFS results of Cu(II)-PDA and Cu oxide standards. The Cu oxide standards show strong backscattering formed by the second shell of Cu atom, but Cu(II)-PDA does not show these backscattering peaks. Chemical structure of Cu(II)-PDA is highly similar to that of the natural melanin containing Cu ions. These results suggest that Cu atom is embedded as an organometallic chelate complexed to organic O terminated catechol groups in PDA structure rather than as Cu inorganic compounds. The morphology of PDA and Cu(II)-PDA was investigated by Scanning electron microscopy (SEM) as shown in (fig 5.2 a,b). First, the structure of PDA was shown a particle-like shape and the size was approximately 100 nm. In previous studies, the synthetic PDA from dopamine oxidation under basic pH has platelet structure and an onion like organization.[5.20] In case of Cu(II)-PDA, however, the particle-like organization was completely lost and a plate-like shape was formed. This formation of plate-like shape can be explained by the fact that Cu ion interferes with the oligomerization of DHI (5,6-dihydroxyindole) units.[5.19] High resolution transmission electron microscopy (HRTEM) was measured to further investigate morphology of Cu(II)-PDA structure as shown in (figure 5. 2c,d). Cu(II)-PDA matrix shows homogeneous, amorphous sheet like structure and contains no aggregated Cu species such as metallic Cu, Cu oxides. It is worth noting that the Cu ions was chelated on dopamine monomer and PDA oligomers in the polymerization process and uniformly distributed in PDA nanostructure. These results confirmed the successful synthesis of metal complexed PDA structure. To investigate the electrocatalytic activity of the PDA and Cu(II)-PDA, cyclic voltammetry was measured by using a rotating disk electrode (RDE) system. The current density vs. potential (*J-E*) curves (Figure. 5.3a) obtained from the RDE measurements show that the current density associated with the HER exponentially increases when the potential is swept from 0 to -0.2 V vs. RHE.

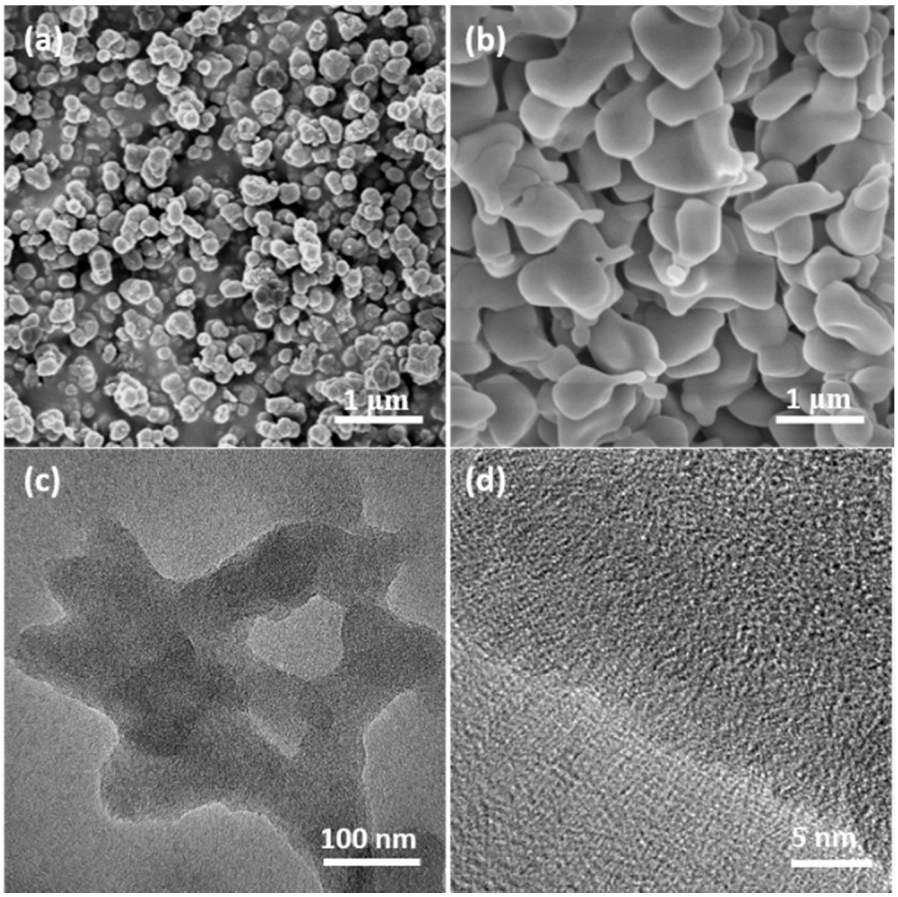

Figure 5. 2. Morphology of PDA, Cu-PDA(II) structure, (a,b) SEM images of PDA, Cu(II)-PDA (c,d) High- resolution TEM images of Cu(II)-PDA

To compare the capability of these materials for HER activity, the potential required to attain a current density of 10 mA cm^{-2} for the HER is defined as overpotential from *J-E* curves (Table 5.1). In addition, RDE measurements of a PDA catalyst as a standard reference sample were obtained. The overpotential for the HER with PDA is -500 mV vs. RHE; this potential is positively (cathodically) shifted by 600 mV relative to that for the bare glassy carbon. Through much research to date[5.21-5.22], PDA is known as proton-electron dual conductors with catechol-quinone functional groups.

These functional groups such as catechol and quinone have been reported to act as proton donor in hydrogen production as well as in proton and electron transport. The HER catalytic activity of these PDA is presumed to be due to the role of catechol-quinone as a proton donor. The HER properties of PDA are further enhanced by incorporating with Cu ion. Interestingly, the *J-E* curve for the Cu(II)-PDA shows the largest negative shift with the overpotential at 10 mA cm^{-2} of -110 mV vs. RHE, indicating a positive shift of 390 mV compared with that of bare PDA. To understand the role of the Cu complex site for HER, different PDA containing various transition metal ion such as Co, Fe, Mn, and Ni was prepared and estimated the catalytic performance (Si fig. 3). To our knowledge, this value is the lowest among Cu-based HER catalysts reported to date and is comparable to those of the best-performing metal-based catalysts at neutral pH[5.2-5.23-5.24] (Table 5.1). This superior catalytic performance of Cu(II)-PDA is further demonstrated by their high stability. Chronoamperometry measurements were performed at -0.05 V vs. RHE, and the obtained current densities are displayed as a function of time in Figure. 5. 3c. The Cu(II)-PDA maintains a current of -5.2 mA cm^{-2} even after 10000 sec. This result indicates that the Cu(II)-PDA exhibit good stability as well as efficient electrocatalytic activity towards the HER under neutral condition.[5.3,5.24-5.35]

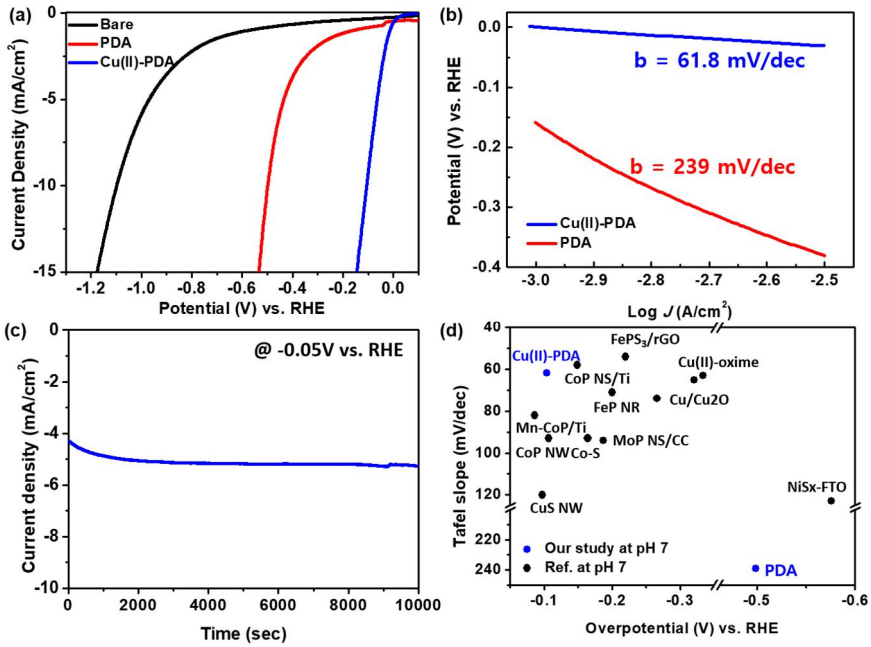

Figure 5. 3. Electrochemical activity of PDA and Cu(II)-PDA on glassy carbon (GC) electrodes in rotating disk electrode (RDE) system (a) Cyclic voltammograms (CV) of PDA, and Cu(II)-PDA on GC. (b) Tafel plots derived from the CV data in (a). (c) Stability test of Cu(II)-PDA. (d) Electrochemical performance of Cu(II)-PDA on a GC electrode and other Non-noble metal based HER catalysts in neutral media. References can be found in the (SI table 1)

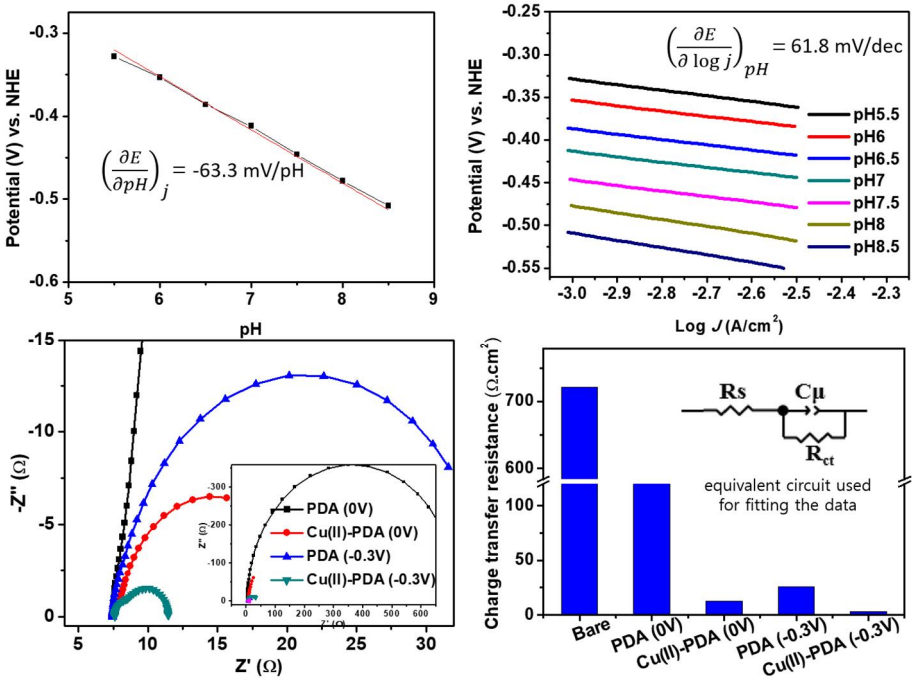

Figure 5. 4. (a) pH dependency test of Cu(Ⅱ)-PDA, (b) Tafel slope transition of Cu(Ⅱ)-PDA depending on pH, (c) Nyquist plot for PDA and Cu(Ⅱ)-PDA at 0 V and -0.3 V vs RHE, (d) Charge transfer resistance of PDA and Cu(Ⅱ)-PDA.

To gain more quantitative insight into the catalytic activity of the Cu(II)-PDA catalysts, the *J-E* curves in Fig. 3a are converted into Tafel plots, in which the potential is plotted as a function of the logarithm of *J*. Owing to solution resistance at the interface between the electrode and electrolyte, the measured potentials compensate for ohmic potential drop (iR) losses. The Tafel slope is defined as the potential increase required to increase the resulting current by one order of magnitude. A Tafel slope of 239 mV dec^{-1} is obtained for PDA, whereas a Tafel slope of 61.8 mV dec^{-1} is obtained for the Cu(II)-PDA (Figure. 5. 2b). The Tafel slope is an inherent property of the catalyst that is determined by the rate-limiting step for the HER. Typically, a

Tafel slope of 120, 40 and 30 mV dec^{-1} indicated that Volmer, Heyrovsky and Tafel determined the rate step respectively. The detailed reaction step is described by the following three equations.

(Volmer step) $H_3O^+ + e^- + * \leftrightarrow H^* + H_2O$ (1)

(Heyrovsky step) $H^* + H_3O^+ + e^- \leftrightarrow H_2 + H_2O + *$ (2)

(Tafel step) $2H^* \leftrightarrow H_2$ (3)

where * is an active site for HER catalysis. The observed Tafel slope of 61.8 mV dec^{-1} for Cu(II)-PDA indicates that Heyrovsky step is rate-determining step.[36]

To evaluate the detailed hydrogen evolution mechanism, a pH dependency test was performed in the pH range between 5.5 and 8.5. The dependence of proton activity on current density is derived as

$$\left(\frac{\partial E}{\partial pH}\right)_j = -\left(\frac{\partial log j}{\partial pH}\right)_E \left(\frac{\partial E}{\partial log j}\right)_{pH} \quad (5)$$

From the pH dependency test, $\left(\frac{\partial \mathrm{E}}{\partial \mathrm{pH}}\right)_j$ is calculated as -63.3 mV/pH (Fig. 4a). Substituting the value of $\left(\frac{\partial \mathrm{E}}{\partial \mathrm{pH}}\right)_j$ and the Tafel slope $\left(\frac{\partial E}{\partial log j}\right)_{pH}$ (Fig. 4b) into equation (5) gave a $\left(\frac{\partial log j}{\partial pH}\right)_E$ value of 1.02, which indicates that the reaction rate has a first-order dependence on the proton activity. As a result, the electrochemical law for Cu(II)-PDA is as follows:

$$i = k_0 (a_{H^+})^{-1.02} e^{\frac{0.5EF}{RT}} \quad (6)$$

where, k_0, a_{H+}, and F are a potential-independent constant, the proton activity, and the Faraday constant, respectively. From this result, it can be assumed that a single electron and single proton are involved in the rate-determining step.

To investigate the origin of the change in the catalytic activity, electrochemical impedance measurements were performed at -0.3 and 0 V vs RHE respectively. A Nyquist plot of a typical impedance result with only one semicircle is shown in Figure. 5. 4c. The single semicircle indicates that the equivalent circuit for the electrocatalysis is characterized by one time constant.

Compared with the bare PDA (26 Ωcm^2), the semicircle observed for the Cu(II)-PDA is much smaller, corresponding to a lower charge-transfer resistance (2.8 Ωcm^2) at -0.3 V vs RHE. The charge-transfer resistance is related to the kinetic barrier energy for faradaic reactions (HER) across the interface between the catalyst and electrolyte. The charge-transfer resistance is also inversely proportional to the exchange current for the faradaic reaction, as described by the Butler-Volmer equation. Consequently, the lower charge-transfer resistance of the Cu(II)-PDA promotes the HER, thus lowering the overpotential. Thus, the impedance analysis verifies the enhanced catalytic properties of the Cu(II)-PDA.

5.3 Conclusion

In this study, polydopamine, which is bio-inspired molecules, and Cu(II)-polydopamine (PDA) derivatives were synthesized by mimicking the mussel adhesive protein and used for the first time as HER electrocatalysts. To investigate the effect of metal ion in polydopamine matrix, we also synthesized PDA derivatives containing various transition metal ions such as Mn (II), Fe (III), Co (II), Ni (II) and Cu (II). Among these catalysts, Cu(II)-PDA show outstanding catalytic performance (η = 104 mV) at neutral pH due to Cu doping active sites. To our knowledge, the Cu(II)-PDA is the best active catalyst based on Cu-based electrocatalyst, and also comparable to non-noble electrocatalyst for HER in neutral pH condition. Our results suggest that organic ligand-transition metal ion complex, inspired by nature, can be applied as a highly efficient electrocatalyst for hydrogen production in neutral condition and also improved in performance through additional molecular engineering.

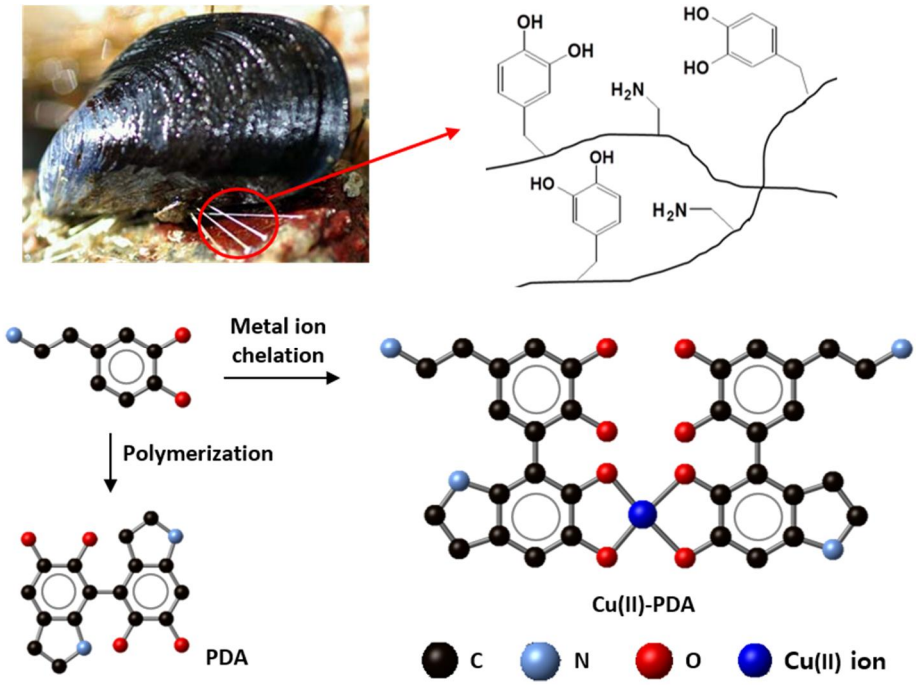

Figure 5. 5. Schematic illustration of proposed structure of polydopamine (PDA) and Copper-complexed PDA (Cu(II)-PDA) as MAPs analogues by oxidative polymerization.

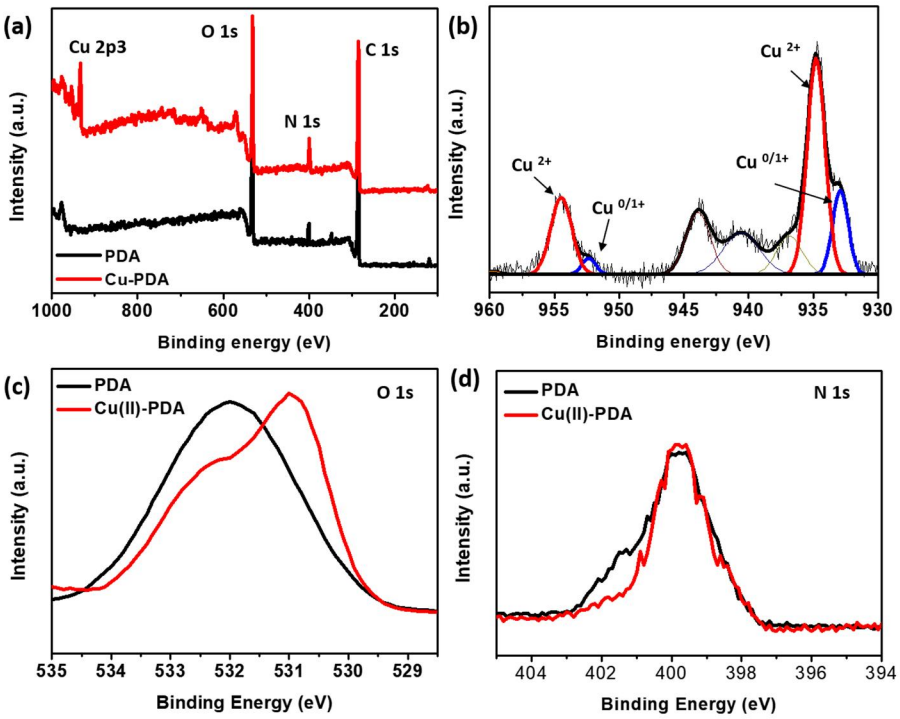

Figure 5. 6. (a) XPS spectra of PDA and Cu(II)-PDA, (b-d) detailed Cu 2p3, O 1s and N 1s XPS peaks of PDA and Cu(II)-PDA

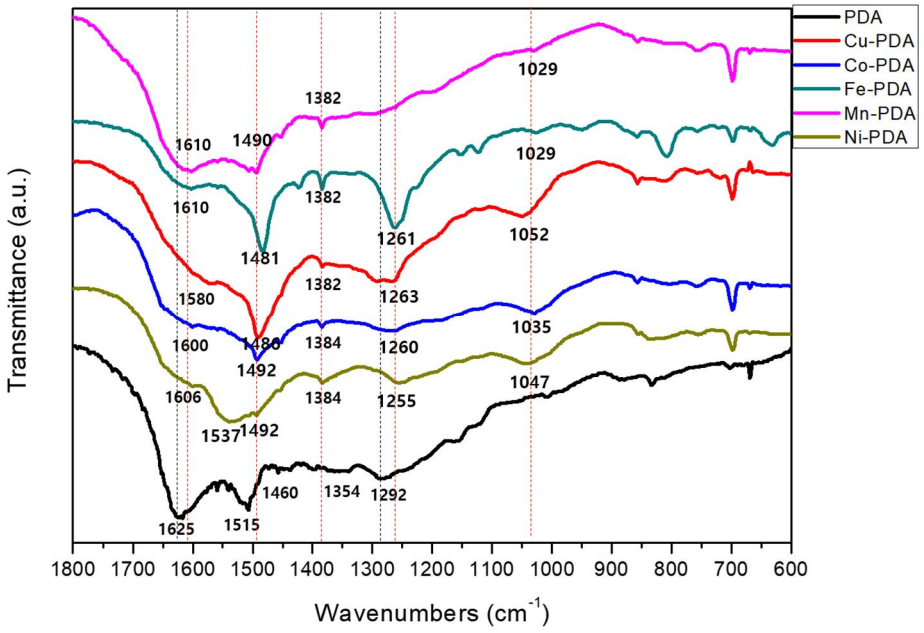

Figure 5. 7. FT-IR spectra of PDA containing various transition metals (Co, Fe, Mn, Ni and Cu)

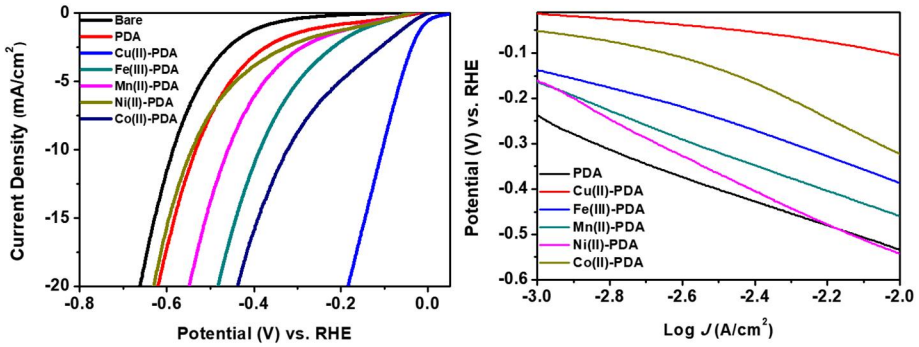

Figure 5. 8. (a) Cyclic voltammograms (CV) of PDA, and various transition metal containing-PDA on GC. (b) Tafel slope derived from the CV data in (a).

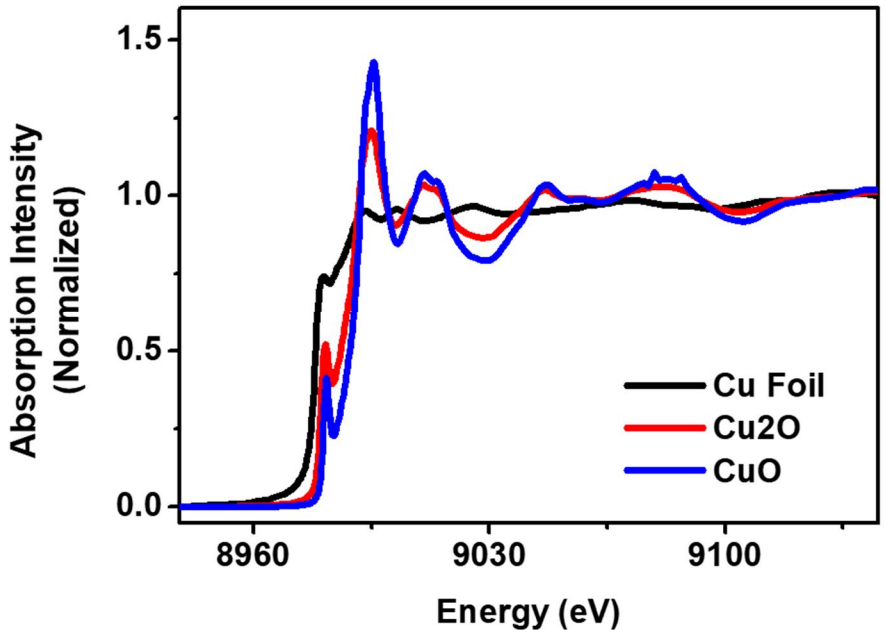

Figure 5. 9. XANES of Cu2O, CuO, and Cu foil.

	Electrolyte	Overpotential (-10mA/cm2)	Tafel slope	Refenece
PDA	**pH 7, Pi 1M**	**499 mV**	**239 mV/dec**	**This study**
Cu(II)-PDA	**pH 7, Pi 1M**	**104 mV**	**61.8 mV/dec**	
Co_9S_8@C	pH 7, Pi 1M	280 mV	NA	ACS Appl. Mater. Interfaces 2015, 7, 980
CoNC/GD	pH 7, Pi 1M	368 mV	207 mV/dec	ACS Appl. Mater. Interfaces 2016, 8, 31083
Co-NRCNT	pH7 Pi 0.1M	540 mV	NA	Angew. Chem. 2014, 126, 4461
CoP nanowire	pH7 Pi 1M	107 mV	93 mV/dec	J. Am. Chem. Soc. 2014, 136, 7587
CoP nanosheet/Ti	pH7 Pi 0.2M	149 mV	58 mV/dec	Chem. Mater. 2014, 26, 4326
Co-S film	pH7 KPi 1M	~164 mV	93 mV/dec	J. Am. Chem. Soc. 2013, 135, 17699
Cu/Cu_2O	pH7 KPi 0.5M	~321 mV (-8 mA/cm2)	65 mV/dec	ACS Catal. 2015, 5, 4115
Cu(II)-EA	pH 7, KPi 0.1M	~738mV	127 mV/dec	Chem. Commun., 2015, 51, 12954
Cu(II)-L complex	pH 7 Pi 0.15M	~920mV	218 mV/dec	ACS Sustainable Chem. Eng. 2017, 5, 7496
Cu_2MoS_4	pH7, Pi 0.1 M	337 mV	NA	Energy Environ. Sci., 2012, 5, 8912
CuS NW	pH 7, Pi 0.2M	97 mV	120 mV/dec	Electrochimica Acta, 2017, 252, 516
Cu(II)-Oxime	pH 7, Pi 0.5M	~334mV	63 mV/dec	ACS Appl. Mater. Interfaces 2016, 8, 30205

FeP/Ti	pH6.5, Pi 1M	102 mV	NA	ACS nano, 2014, 8, 11, 11101 (2004)
FeP Nanorod	pH 7, Pi 1M	200 mV	71 mV/dec	Acs catal, 2014, 4, 4065
$FePS_3$/rGO	pH 7 Pi 0.5M	220 mV	54 mV/dec	ACS Energy Lett. 2016, 1, 367
Mn-doped CoP/Ti	pH 7, Pi 1M	86 mV	82 mV/dec	ACS Catal. 2017, 7, 98
Mo_2C@NC	pH 7, Pi 0.1M	156mV	NA	Angew. Chem. 2015, 127, 10902
Mo_2C-GNR	pH7, Pi 1M	266 mV	74 mV/dec	ACS Sustainable Chem. Eng. 2016, 4, 6313
MoP nanosheet/CC	pH7, Pi 1M	187 mV	94 mV/dec	Applied Catalysis B: Environmental, 2016, 196, 193
NiSx-FTO	pH7, Pi 1M	576 mV	123 mV/dec	Langmuir 2016, 32, 12005

*: Values were measured and extrapolated by our group referring to the figures and data from the references.

Table 5.1. Comparison of the electrocatalytic activity of PDA, Cu(II)-PDA reported here and some representative non-noble metal based catalysts for HER in neutral media.

Bibliography

5.1. J. A. Turner, *Science*, 2004, **305**, 972-974..

5.2. T. Liu, X. Ma, D. Liu, S. Hao, G. Du, Y. Ma, A. M. Asiri, X. Sun and L. Chen, *ACS Catalysis*, 2017, **7**, 98-102.

5.3. J. Tian, Q. Liu, A. M. Asiri and X. Sun, *Journal of the American Chemical Society*, 2014, **136**, 7587-7590.9.4. U. Sim, T.-Y. Yang, J.

5.5. X. Zou, X. Huang, A. Goswami, R. Silva, B. R. Sathe, E. Mikmeková and T. Asefa, *Angewandte Chemie*, 2014, **126**, 4461-4465.

5.6. X. Hu, B. S. Brunschwig and J. C. Peters, *Journal of the American Chemical Society*, 2007, **129**, 8988-8998.

5.7. L. Gan, T. L. Groy, P. Tarakeshwar, S. K. S. Mazinani, J. Shearer, V. Mujica and A. K. Jones, *Journal of the American Chemical Society*, 2015, **137**, 1109-1115

5.8. P.-A. Jacques, V. Artero, J. Pécaut and M. Fontecave, *Proceedings of the National Academy of Sciences*, 2009, **106**, 20627-20632

5.9. J. Du, J. Wang, L. Ji, X. Xu and Z. Chen, *ACS Applied Materials & Interfaces*, 2016, **8**, 30205-30211.

5.10. X. Liu, S. Cui, Z. Sun and P. Du, *Chemical Communications*, 2015, **51**, 12954-12957

5.11. H. Lee, S. M. Dellatore, W. M. Miller and P. B. Messersmith, *Science (New York, N.Y.)*, 2007, **318**, 426-430

5.12. M. d'Ischia, A. Napolitano, A. Pezzella, P. Meredith and T. Sarna, *Angewandte Chemie International Edition*, 2009, **48**, 3914-3921.

5.13. J. H. Waite and X. Qin, *Biochemistry*, 2001, **40**, 2887-2893

5.14. H. Lee, N. F. Scherer and P. B. Messersmith, *Proceedings of the National Academy of Sciences*, 2006, **103**, 12999-13003

5.15. E. Degtyar, M. J. Harrington, Y. Politi and P. Fratzl, *Angewandte Chemie International Edition*, 2014, **53**, 12026-12044

5.16. M. J. Sever and J. J. Wilker, *Dalton Transactions*, 2006, DOI: 10.1039/B509586G, 813-822

5.17. L. Yang, J. Kong, D. Zhou, J. M. Ang, S. L. Phua, W. A. Yee, H. Liu, Y. Huang and X. Lu, *Chemistry – A European Journal*, 2014, **20**, 7776-7783.

5.18. A. B. Mostert, B. J. Powell, F. L. Pratt, G. R. Hanson, T. Sarna, I. R. Gentle and P. Meredith, *Proceedings of the National Academy of Sciences*, 2012, **109**, 8943-8947.

5.19. M. Zdybel, B. Pilawa, E. Buszman and D. Wrześniok, *Chemical Physics Letters*, 2013, **556**, 278-286.

5.20. V. Ball, J. Gracio, M. Vila, M. K. Singh, M.-H. Metz-Boutigue, M. Michel, J. Bour, V. Toniazzo, D. Ruch and M. J. Buehler, *Langmuir*, 2013, **29**, 12754-12761.

5.21. A. B. Mostert, B. J. Powell, I. R. Gentle and P. Meredith, *Applied Physics Letters*, 2012, **100**, 093701.

5.22. V. Gargiulo, M. Alfe, R. D. Capua, A. R. Togna, V. Cammisotto, S. Fiorito, A. Musto, A. Navarra, S. Parisi and A. Pezzella, *Journal of Materials Chemistry B*, 2015, **3**, 5070-5079.

5.23. D. Merki, H. Vrubel, L. Rovelli, S. Fierro and X. Hu, *Chemical Science*, 2012, **3**, 2515-2525.

5.24. Z. Pu, Q. Liu, P. Jiang, A. M. Asiri, A. Y. Obaid and X. Sun, *Chemistry of Materials*, 2014, **26**, 4326-4329.

5.25. Y. Çimen, A. W. Peters, J. R. Avila, W. L. Hoffeditz, S. Goswami, O. K. Farha and J. T. Hupp, *Langmuir*, 2016, **32**, 12005-12012.

5.26. C. Di Giovanni, W.-A. Wang, S. Nowak, J.-M. Grenèche, H. Lecoq, L. Mouton, M. Giraud and C. Tard, *ACS Catalysis*, 2014, **4**, 681-687.

5.27. P. D. Tran, M. Nguyen, S. S. Pramana, A. Bhattacharjee, S. Y. Chiam, J. Fize, M. J. Field, V. Artero, L. H. Wong, J. Loo and J. Barber, *Energy & Environmental Science*, 2012, **5**, 8912-8916.

5.28. Y. Liu, G. Yu, G.-D. Li, Y. Sun, T. Asefa, W. Chen and X. Zou, *Angewandte Chemie International Edition*, 2015, **54**, 10752-10757.

5.29. J. Miao, F.-X. Xiao, H. B. Yang, S. Y. Khoo, J. Chen, Z. Fan, Y.-Y. Hsu, H. M. Chen, H. Zhang and B. Liu, *Science Advances*, 2015, **1**..

5.30. W. Gao, Y. Shi, Y. Zhang, L. Zuo, H. Lu, Y. Huang, W. Fan and T. Liu, *ACS Sustainable Chemistry & Engineering*, 2016, **4**, 6313-6321.

5.31. W. Cui, Q. Liu, Z. Xing, A. M. Asiri, K. A. Alamry and X. Sun, *Applied Catalysis B: Environmental*, 2015, **164**, 144-150.

5.32. C. Tang, Z. Pu, Q. Liu, A. M. Asiri and X. Sun, *Electrochimica Acta*, 2015, **153**, 508-514.

5.33. L. Ji, L. Zhu, J. Wang and Z. Chen, *Electrochimica Acta*, 2017, **252**, 516-522.

5.34. Y. Liang, Q. Liu, A. M. Asiri, X. Sun and Y. Luo, *ACS Catalysis*, 2014, **4**, 4065-4069.

5.35. A. T. Garcia-Esparza, D. Cha, Y. Ou, J. Kubota, K. Domen and K. Takanabe, *ChemSusChem*, 2013, **6**, 168-181.

5.36. B. E. Conway and G. Jerkiewicz, *Electrochimica Acta*, 2000, **45**, 4075-4083.

Chapter 6. Concluding remarks

Development of sustainable energy sources is a significant issue to fulfill growing demand in world energy consumption. Among the various types of sustainable energy, hydrogen is the most promising sustainable energy source with a high energy efficiency. The discovery of efficient catalysts represents the most significant issue for the implementation of photoelectrochemical (PEC) hydrogen production. A critical requirement for efficient catalysts in a PEC cell is not only an ability to improve the kinetics of a chemical reaction but also a durability against electrochemical and photo-induced degradation. Usually, noble metals, such as platinum, exhibit superior performance in these requirements; however, the high cost issue is the biggest barrier to widespread practical use. To overcome this critical and long-standing technical barrier, We have focused on an intense search for efficient, durable, and inexpensive alternative catalysts. We studied the field of the graphene derived-catalyst for HER in PEC cell that have never been made before. Inspired by biomolecular approach, we also have made a breakthrough in the limit of recent photo-to-current efficiency through the incorporation of a non-noble transition metal into carbon-based catalysts.

Carbon-based nanomaterials have emerged as promising candidate catalyst for HER. The preparation of carbon-based catalysts represents an important research way in the search for non-precious, environmentally friendly, and durable catalysts. Especially, graphene possesses excellent transmittance and superior intrinsic carrier mobility, thus there have been several attempts to use graphene as a co-catalyst or supporting material. It has been reported that reduced graphene oxide containing catalytic active materials exhibited improved activity in HER, oxygen evolution reactions, and oxygen reduction reactions. In most cases, the role of carbon materials is limited to an electrical

conducting substrate or a supporter that enhances the performance of other decorated active catalysts. There is no previous study of monolayer graphene for hydrogen production. For the first time, we demonstrated new possibilities for monolayer graphene from CVD method as an electrocatalyst for efficient HER and found that atomic defect engineering such as nitrogen doping through treatment with N_2 plasma improved the catalytic activity. This study has also attracted interests to the materials and chemical society in that it has demonstrated the role of carbon-based catalysts and N-GQSs with comprehensive electrochemical analysis as well as the first demonstration of monolayer graphene as the HER catalyst.

Furthermore, carbon nanosheet is synthesized by polydopamine, which are natural adhesive proteins secreted by marine mussels. Based on the understanding about the synthesis of the biomimetic carbon platform, earth-abundant metal active sites have been incorporated with high controllability and tunability, which results in a further decrease in kinetic overpotential. Cu(II)-polydopamine (PDA) derivatives were synthesized by mimicking the mussel adhesive protein and used for the first time as HER electrocatalysts. To investigate the effect of metal ion in polydopamine matrix, we also synthesized PDA derivatives containing various transition metal ions such as Mn (II), Fe (III), Co (II), Ni (II) and Cu (II). Among these catalysts, Cu(II)-PDA show outstanding catalytic performance (η = 104 mV) at neutral pH due to Cu doping active sites. To our knowledge, the Cu(II)-PDA is the best active catalyst based on Cu-based electrocatalyst, and also comparable to non-noble electrocatalyst for HER in neutral pH condition. This significant enhancement achieved in this study emphasizes the strategies for the application of bioinspired materials as the HER catalyst. My bioinspired catalysts paradigm can revolutionize the catalyst materials that have traditionally made by alloying inorganic metal composite or have had little interest in surrounding carbon platform, opening the way to the design of atomic-scale controlled

catalysts, materials inspired from biomolecular precursor approach, and learning design rules for interfacing semiconductor and catalysts.

My synthetic bioinspired HER catalyst is also highly transparent and is applicable to the co-catalyst for the PEC cell. The results indicate the applied bias photon-to-current efficiency of 2.29%, which is higher than any other carbon-based PEC catalysts reported to date. In PEC cell system, negative effects from metal-based catalysts should be considered: reflection by the overlaid catalyst, an unfavorable band structure such as a Schottky barrier, photocorrosion, and recombination sites at the interface. To design catalysts for PEC water splitting, the optical properties, stability, and interfacial issues must be comprehensively considered. Silicon, the most promising photocathode material for absorbing of large part of visible spectrum, precise controllability, and its abundancy, however, cannot durably operate in aqueous electrolyte because of surface oxidation. Thus, passivation of silicon surface is essential for the durable operation of the silicon photocathode in neutral water. My transparent carbon catalysts on silicon acts as a passivation layer against surface oxidation without attenuating the photon incidence. Controlling a surface structure of the light-absorbing photoelectrode and the deposition with the co-catalyst also represent a significant step toward enhancing the hydrogen production. This transparent catalyst with a capability of passivation effect can result in a paradigm shift for catalytic materials research and discovery for energy application.

The significant meaning of this research is the construction of transparent catalyst that only consists of carbon materials and the possibility of extension to a variety of biomimetic HER catalysts with excellent activity. This synthetic approach would allow development of catalysts with unique and highly tunable properties with broad energy applications as well as the efficient solar-driven hydrogen production.

Publication List

Papers:

1. **Junghyun An**, Kyoungsuk Jin, Sung Eun Jerng, Nark-Eon Sung, Sun Hee Kim, Uk Sim, and Ki Tae Nam, "Bioinspired Copper Coordinated Polydopamine-melanin Catalyst for Efficient Hydrogen Evolution at Neutral pH.", in preparation.
2. **Junghyun An**, Kyoungsuk Jin, Uk Sim, and Ki Tae Nam, "Electrochemical Analysis of Carbon Nanosheet Catalyst on Silicon Photocathode for Hydrogen Generation ", Bulletin of the Korean Chemical Society under revision
3. Kyoungsuk Jin,† **Junghyun An,†** Junsang Moon, Heonjin Ha, Hyo-Yong Ahn,Sun Hee Kim, Uk Sim, and Ki Tae Nam, "Biomimetic Iron Sulfur/Carbon-based Catalyst for Efficient and Stable Hydrogen Production across all pH Conditions" in preparation
4. Joonhee Moon†, **Junghyun An†**, Uk Sim, Sung-Pyo Cho, Jin Hyoun Kang, Chul Chung, Jung-Hye Seo, Jouhahn Lee, Ki Tae Nam, and Byung Hee Hong "One-Step Synthehsis of N-doped Graphene Quantum Sheets from Monolayer Graphene by Nitrogen Plasma", Advanced Materials 26, 3501 (2014)
5. Uk Sim†, Joonhee Moon†, **Junghyun An**, Hyo-Yong Ahn, Dong Jin Kim, Insu Jo, Byung Hee Hong and Ki Tae Nam, "Double-layer Graphene Outperforming Monolayer as Catalyst on Silicon Photocathode for Hydrogen Production", *ACS Appl. Mater. Interfaces. 9 (4), 3570 (2017)*
6. Uk Sim†, Joonhee Moon†, **Junghyun An,** Jin Hyoun Kang, Sung Eun Jerng, Junsang Moon, Sung-Pyo Cho, Byung Hee Hong and Ki Tae Nam, "N-doped Graphene Quantum Sheets on Silicon Nanowire Photocathode for Hydrogen Production", Energy & Environmental Science 8, 1329 (2015)

7. Ki Dong Yang, Yoonhoo Ha, Uk Sim, **Junghyun An**, Chan Woo Lee, Kyoungsuk Jin, Younghye Kim, Jimin Park, Jung Sug Hong, Jun Ho Lee, Hye-Eun Lee, Hui-Yun Jeong, Hyungjun Kim, Ki Tae Nam, "Graphene Quantum Sheet Catalyzed Silicon Photocathode for Selective CO2 Conversion to CO", Advanced Functional Materials. 26, 233 (2015)
8. Uk Sim†, Tae-Youl Yang†, Joonhee Moon†, **Junghyun An**, Jinyeon Hwang, Jung-Hye Seo, Jouhahn Lee, Kye Yeop Kim, Joohee Lee, Seungwu Han, Byung Hee Hong, and Ki Tae Nam, "N-doped Monolayer Graphene Catalyst on Silicon Photocathode for Hydrogen Production", *Energy & Environmental Science* **6**, 3658-3664 (2013)
9. Vinayak S. Kale, Uk Sim, Jiwoong Yang, Kyoungsuk Jin, Sue In Chae, Woo je Chang, Arun Kumar Sinha, Heonjin Ha, Chan-Cuk Hwang, **Junghyun An**, Hyo-Ki Hong, Zonghoon Lee, Ki Tae Nam, Taeghwan Hyeon, Small. 13, 1603893 (2017).

Patent:

1. Uk Sim, Joonhee Moon, **Junghyun An**, Ki Tae Nam, and Byung Hee Hong, "N-doped Graphene Quantum Sheets Catalyst for Hydrogen Evolution Reaction", (No. 1020150143133 (2015.12.23))

초 록

전 세계적인 에너지 소비량의 급증으로 인하여 신 재생 에너지의 필요성은 더욱더 중요한 이슈로 자리매김하고 있다. 현재 에너지원은 주로 화석연료를 사용하는데, 화석연료의 고갈과 최근 이산화 탄소 배출로 인한 지구 온난화 및 미세먼지에 대한 문제로 인하여 자연친화적인 신 재생에너지에 대한 갈망은 더욱 증가하고 있다. 또한 이를 대체하는 에너지원으로 원자력 발전을 예를 들 수 있다. 하지만 이 역시 최근 후쿠시마 원전 사고로 안전성에 큰 문제가 지적되었고, 우리나라 역시 경주 지진을 통해서 원전 사고 안전 지대가 더 이상 아니다라는 주장이 있다. 독일의 경우, 2000년 초반부터 탈 원전 정책을 시행하였고, 이와 동시에 태양광, 바이오에너지 등을 통해서 현재 30%의 에너지 공급을 하고 있다. 하지만 현재는 청정 에너지의 기술적 한계로 인하여, 서로의 단점을 극복하는 다각도의 청정 에너지 기술이 요구된다. 이러한 이유로 최근 수소에너지가 새로운 대체 에너지원으로 주목을 받고 있다. 수소에너지는 반응 생성물이 물과 열이며 이산화 탄소 배출이 없어 친환경적이다. 현재 전체 수소 에너지의 약 96%는 기체 개질(gas reforming)을 통해 얻어지고 4% 정도가 물 전기분해 또는 광전기화학적 물분해를 통해 얻어지고 있다. 그러나 기체 개질은 수소 에너지를 생산하는 과정에서 비친환경 물질인 이산화탄소를 부산물을 생성해 낼 뿐 아니라, 고온 고압과 같은 어려운 조건에서 반응이 진행되어 위험성을 지니고 있다. 이와는 달리, 물 전기 분해 또는 광전기화학적 물분해는 수소를 생산하는 과정에서 오직 산소만을 부산물로 만들어내고 상온에서도 반응이 가능하기 때문에

최근 들어 주목을 받고 있는 추세이다. 따라서 저렴한 가격으로 수소 에너지를 생산하기 위해 물 전기분해 관련 연구의 필요성이 대두되고 있다. 하지만 현재 수소 생산 비용은 상용화된 기체 개질을 통한 방법보다는 여전히 비싸므로 이를 낮추려는 노력이 중요하다. 지금까지 개발된 효율 높은 촉매들은 귀금속 기반의 촉매들로서 가격 경쟁력 확보가 시급하다. 따라서, 이러한 전기화학적 반응을 이용한 수소 생산에 있어서 효율적인 촉매의 개발은 매우 중요하며, 시급히 해결해 나가야 할 문제이다.

가장 단순한 탄소 기반 플랫폼의 형태로 CVD-monolayer 및 질소 플라즈마를 이용한 질소 도핑된 그래핀 양자 시트의 수소 발생 반응 촉매특성이 있음을 최초로 확인을 하였고, 수소 발생 반응 메커니즘을 분석하였다. 실리콘 광전극에 적용하여, 입사광의 손실 없이 효과적인 투명 조촉매로 작용할 뿐 아니라, 실리콘의 산화를 방지하여 장기안정성에 뛰어난 특성을 보임을 확인하였다.

촉매의 수소 발생 반응 사이트를 좀더 체계적으로 조절하기 위해 플라즈마 처리를 도입하게 되었고, 질소 도핑 및 결함 사이트를 조절하여 특성을 비약적으로 향상 시켰으며, 플라즈마 처리 과정에서,

지금까지 탄소 기반의 그래핀 촉매 연구에서 배운 교훈을 바탕으로, 좀 더 효과적인 촉매를 디자인하기 위해, 그 후보군 중의 하나로써, 자연계에 존재하는 홍합으로부터 분비되는 접착 단백질을 구성하는 polydopamine이라는 물질에 주목하였는데, 이 물질은 접착력에 관여하는 catechol 작용기로 인해 수용액상에서 표면 특성에 관계없이 다양한 표면을 매우 안정하게 형성하며, carbonization 후에는 전도성 또한 매우 뛰어난 특성을 보일 뿐 아니라, metal ion과도 잘 결합하여 다양한 melanin 구조체를 합성할

수 있는 장점을 가진다. 우리는 먼저 transition metal Cu로 구성된 metal active sites를 디자인하고, 성능을 극대화 할 수 있는 플랫폼 역할을 할 수 있는 군을 탐색하여, 두 성분들이 최적의 구성비율을 가지고 분포된 catalyst를 디자인하여 합성하고자 한다. 이러한 Biomimetic polydopamine을 기반으로, dopa-HCl과 Cu 전구체 소스를 이용하여, 매우 간단한 방법으로 polydopamine이 둘러싸인 새로운 구조의 Cu-Polydopamine Catalyst를 합성하였다. 해당 촉매의 수소 발생 촉매 특성을 살펴 본 결과, 중성 pH 범위에서 수소 발생 능력이 매우 뛰어날 뿐 아니라, 안정성도 좋은 것을 확인할 수 있었고, 지금까지 보고된 Cu 계열의 촉매들과 비교하여 수소발생 특성이 가장 뛰어남을 확인하였다. 효과적인 성능의 원인을 파악하기 위해, Impedance 분석을 통해 metal active site를 감싸고 있는 polydopamine이 반응에 필요한 electron을 효과적으로 transfer를 할 수 있게 도와주는 것을 확인하였고, pH 의존도 실험을 통해, 해당 촉매의 Proton coupled electron transfer 능력이 매우 뛰어남을 확인할 수 있었을 뿐만 아니라,

결론적으로, 자연계의 생체 촉매의 구조 및 성분을 모방하여, 그 교훈으로부터 뛰어난 특성과 안정성을 가진 비귀금속 탄소기반 수소 발생 반응 촉매 개발을 달성해 낼 수 있었다.

주요어: 광전기화학셀, 탄소, 촉매, 생체모방, 물분해, 수소발생
학 번: 2012-30162